
This manuscript is a preprint and has not undergone peer-review. Please note that subsequent versions of this manuscript may have different content. If accepted, the final version of this manuscript will be available via the 'Peer-reviewed Publication DOI' link on the right-hand side of this webpage. Please feel free to contact any of the authors, we welcome feedback!

1 Transformation of dense shelf water cascade into turbidity
2 currents: insights from high-resolution geophysical datasets

3 Nan Wu^{1*}, Guangfa Zhong¹, Yakufu Niyazi², Biwen Wang¹, Harya D. Nugraha³,

4 Michael J. Steventon⁴

5 ¹State Key Laboratory of Marine Geology, Tongji University, 1239 Siping Road,
6 Shanghai, 200092, China

7 ²Minderoo-UWA Deep-Sea Research Centre, School of Biological Sciences and UWA
8 Oceans Institute, The University of Western Australia, Perth, WA 6009, Australia

9 ³Center for Sustainable Geoscience, Universitas Pertamina, Jakarta, 12220, Indonesia

10 ⁴Shell Research, Shell Centre, London, SE1 7NA, UK

11 *Email: nanwu@tongji.edu.cn

12

13 **ABSTRACT**

14 Dense shelf water cascade (DSWC) is a common oceanographic phenomenon on many
15 continental shelves. Previous studies indicate that the DSWC could shape seabed
16 physiography and carry seawater, sediment, and organic carbon a long distance from
17 the continental shelf to the basin floor. However, it remains enigmatic how these
18 DSWC's interact with seabed geomorphology and travel long distances from the
19 shallow to deep marine environments. In this study, we employed high-resolution
20 multibeam bathymetry, 2D and 3D seismic reflection, core description, and sediment
21 grain size data from the Gippsland Basin, southeast offshore Australia. The continental
22 shelf of the central Gippsland Basin stores sediment supplied by the along-shelf

23 transported DSWC. By calculating the sediment motion threshold, we demonstrate
24 that the DSWC is capable of entraining sediment from, and forming dense bottom
25 nepheloid layers above, the seabed. Seismic reflection data reveal that cyclic steps are
26 common on the shelf and slope, indicating a downslope-transported, supercritical
27 current-dominated environment. Core observation and grain size analyses reveal that
28 coarse-grained, Ta-typed turbidites are the major facies, indicating the presence of
29 high-intensity downslope-traversing turbidity currents. Thus, supercritical turbidity
30 currents are the dominant sedimentary process in the central Gippsland Basin. We
31 illuminate that DSWC can interact with pre-existing seabed bathymetry created by a
32 buried submarine landslide, resuspending sediment and igniting downslope-
33 transported turbidity currents. The presence of numerous cyclic steps indicates that
34 the turbidity current can evolve into a supercritical regime upon ignition, leaving
35 complex seabed geomorphology and allowing the forming currents to travel across the
36 shelf and extend more than 80 km down the lower slope. As revealed by our literature
37 review, we imply that the transformation of DSWC into turbidity currents should be a
38 common sedimentary process on outer continental shelves globally, significantly
39 sculpting the seabed morphology and facilitating sediment and other marine particles
40 transportation from shallow to deep sea.

41 Keywords: Dense shelf water cascade (DSWC), Current transformation, Turbidity-
42 current initiation, Gippsland Basin

43

44 1. INTRODUCTION

45 Along the continental shelves, seasonal evaporation during summer and cooling
46 during winter can generate a cross-shelf density gradient that drives denser seawater
47 transport seawards along the seabed (Ivanov et al., 2004; Canals et al., 2006). This
48 process is defined as a dense shelf water cascade (hereafter DSWC). The DSWC is a
49 climate-driven oceanographic phenomenon prominent throughout the tropical to the
50 high-latitude continental margins (Figure 1A; Ivanov et al., 2004; Amblas and
51 Dowdeswell, 2018; Mahjabin et al., 2020; Gales et al., 2021). The DSWC has been
52 repeatedly measured and well-studied by both long-term and high-frequency in situ
53 measurements in physical oceanography observations (i.e. Canals et al., 2006; Puig et
54 al., 2008; Canals et al., 2009). Once the DSWC is initiated, it sinks and overflows the
55 outer shelf area under the influence of gravity, cascading downslope until it reaches
56 its density equilibrium depth (also known as neutral density level; Figure 1B)
57 (Fohrmann et al., 1998; Canals et al., 2009). Results indicate the DSWC can travel more
58 than 10,000 km along the coastline and descends more than 1000 m down the slope
59 and eventually flooding the basin floor (Figure 1B; Ivanov et al., 2004; Canals et al.,
60 2009; Mahjabin et al., 2020). When transported along the shelf, DSWC can travel at a
61 high speed (i.e. 1.2 m/s) and is highly erosive (Canals et al., 2006; Puig, 2017). For
62 example, the DSWC can dislodge a c. 400 kg anchor at least 3 km away from its mooring
63 position, and polish the rusty iron of the train wheel very shiny through continuous
64 sandblasting associated with the powerful cascading currents (Puig et al., 2008).

65

66 The DSWC can affect a large portion of the seabed, induce erosion and deposition, and

67 generate bottom nepheloid layers (zones) that contain significant amounts of
68 suspended sediments and subsequently produce fast travelling gravity flows (Figure
69 1B; Canals et al., 2006; Puig, 2017). At specific locations, canyons are often the major
70 conduits and determine the paths and spreading conditions for the DSWC (Canals et
71 al., 2006; Morrison et al., 2020; Gales et al., 2021). The DSWC has proved to be an
72 effective seabed-sculpting agent and is capable of transferring large amounts of water
73 and heat, sediments, organic carbon, marine pollutants and nutrients from the shallow
74 marine to the deep ocean (Canals et al., 2006; Puig et al., 2008; Canals et al., 2009).
75 Therefore, the DSWC plays an important role in global deep-ocean circulation,
76 sediment source-to-sink, earth's climate system, and carbon and biogeochemical
77 cycles (Amblas and Dowdeswell, 2018).

78

79 Despite the extensive existing literature, some important questions remain to be
80 addressed. Firstly, the process of how DSWC produces gravity flows and shape seabed
81 geomorphology is still poorly understood (Canals et al., 2006; Talling, 2014). Secondly,
82 the reasons for the DSWC spreading over a considerable distance across the shelf and
83 even reaching the lower slope remain unclear. Here we attempt to unravel these
84 important, yet under-explored aspects of DSWC, by presenting observations based on
85 high-resolution bathymetric multibeam, seismic reflection, piston core and sediment
86 grain size datasets from the offshore Gippsland Basin, Australia. The occurrence of the
87 DSWC has brought a large amount of sediment and resulted in extremely complex
88 seabed geomorphology in the central Gippsland Basin (Godfrey et al., 1980; Tomczak,

89 1985; Mitchell et al., 2007b). The complex seabed geomorphology reflects the action
90 of a range of oceanographic and sedimentary processes at multiple spatiotemporal
91 scales. Therefore, the central region of the Gippsland Basin provides an ideal place to
92 investigate the remaining questions we raised above. We revealed that the DSWC can
93 interact with pre-existing seabed depressions caused by deposited submarine
94 landslide, igniting turbidity currents and leaving erosional bedforms on the seabed.
95 We highlight that the transformation of the DSWC into turbidity currents is an
96 underappreciated sedimentary process that should be common on outer continental
97 shelves globally. The transition from the DSWC to the turbidity current is crucial to
98 understanding the evolution of seabed geomorphology through time, as well as the
99 mechanisms that account for the long-distance transportation of the DSWC under the
100 influence of dynamic oceanographic processes.

101

102 2. GEOLOGICAL SETTING

103 2.1 The Gippsland Basin

104 The offshore Gippsland Basin is dominated by a cool-water carbonate system located
105 on SE Australia's passive margin, between the mainland of Australia and Tasmania
106 (Figures 2A, 2B; Rahmanian et al., 1990). It is one of Australia's most prolific
107 hydrocarbon provinces, fisheries, and potential carbon storage, and holds a number of
108 other potential marine resource applications (Rahmanian et al., 1990; Mitchell et al.,
109 2007a; Mitchell et al., 2007b). The Gippsland Basin belongs to a series of rift basins
110 formed along the southern margin of the Australian plate, due to the separation of

111 Antarctica and Australian continents during the breakup of Gondwana in the Mesozoic
112 (Colwell et al., 1993). Since the Pleistocene, the Gippsland Basin has been detached
113 from major river sources, allowing the development of a cool water carbonate
114 province with minimal terrigenous input (Mitchell et al., 2007b). The margin of the
115 Gippsland Basin is dominated by a c. 100 km wide embayment, and the SE margin of
116 the basin is floored by c. 120 km long and 15-70 km wide, ESE-trending Bass Canyon
117 system (Figures 2A, 2B). The Bass Canyon is one of the world's largest submarine
118 canyons and constitutes the SE boundary of the Gippsland Basin (Mitchell et al.,
119 2007b). The Bass Canyon has acted as a major conduit and key element in the source-
120 to-sink system in the SE Australian area since the Late Cretaceous (approximately
121 80Ma; Hill et al., 1998). At present, it still transfers sediments, oxygen, nutrients,
122 pollutants, and organic matter from the canyon head to the Tasman Abyssal Plain at
123 almost 4500 m water depth (Figure 2B).

124

125 2.2 Climate and oceanography

126 The Bass Strait is a shallow (water depth range from 40-60 m) coastal sea between
127 mainland Australia and Tasmania, connecting the Great Australian Bight in the west
128 and the Tasman Sea in the east (Figure 2A; Tomczak, 1985; Lavering, 1994). In winter,
129 the shallow Bass Strait imposes a limit on the penetration of thermal convection, and
130 as a consequence, Bass Strait seawater cools rapidly and has a higher salinity than that
131 of the surface layer in the Tasman Sea (Lavering, 1994). Therefore, when seawater
132 leaves the Bass Strait on its eastern side, it has a prominent density contrast against

133 the Tasman Sea water (Tomczak, 1985). As a consequence, cold, denser Bass Strait
134 seawater can flow into and sink beneath the warmer, fresher water of the Gippsland
135 shelf, generating the northeast-flowing Bass Cascade Current (hereafter BCC) which
136 sinks to the 200-400 m isobaths and extends more than tens of kilometres (Figure 2B;
137 Godfrey et al., 1980; Li et al., 2005; Mitchell et al., 2007b). Observations from the
138 ocean bottom stations have revealed that the BCC is the densest seawater offshore SE
139 Australia, it is active every year and is with an average transport rate of 1.0 Sverdrups
140 (Sv; $1\text{Sv}=10^6 \text{ m}^3/\text{s}$) (Middleton and Bye, 2007). The transportation of BCC has
141 transported significant quantities of water and sediments and spread along the shelf
142 edge over a long distance (Boland, 1971). For example, distinctive temperature-salinity
143 anomalies are found at 200-800 m depth in the Tasman Sea, most likely caused by Bass
144 Strait seawater penetration (Figure 2C; Boland, 1971). In the Gippsland Basin, the
145 central continental shelf is dominated by the Westerly wind throughout the year
146 (especially in winter; Figure 2B; Li et al., 2005). The eastward-flowing Westerly wind
147 flows at 10-30 km/h with maximum gusts reaching 100 km/h. Therefore, the Westerly
148 wind has created a moderate to high energy wave-dominated environment and a
149 robust NE-transported Ekman Transport Flow (ETF) in a water depth of c. 200-300 m
150 (Figure 2B; Mitchell et al., 2007a; O'Brien et al., 2018). The East Australia Current (EAC)
151 is a western boundary current that carries warm equatorial waters and flows
152 southward adjacent to Australia's southeast coast (Figure 2B, 2D). It is up to 500 m
153 deep and 100 km wide, occasionally extending far enough south to reverse the
154 movement of water in the Gippsland Basin during summer months (Li et al., 2005).

155 Therefore, the combination of seasonal northward flowing BCC, the southward flowing
156 EAC, and northeast flowing ETF have jointly controlled the oceanography and
157 sedimentation along SE Australia's continental margin.

158

159 3. DATASET AND METHODOLOGY

160 The datasets available for this study include multibeam bathymetry data with a
161 coverage area of c. 250,000 km², 2D and 3D seismic reflection data with a coverage
162 area of c. 1700 km², with lithology control provided by six-piston core samples (Figures
163 2B, 3A).

164

165 3.1 Multibeam bathymetry

166 Multibeam bathymetry data for this study is sourced and can be downloaded from
167 Geoscience Australia's Marine data portal (<http://marine.ga.gov.au>). The dataset is
168 compiled from multiple bathymetric surveys and gridded at 50x50 m; hence,
169 geomorphological features smaller than 50 m across cannot be differentiated. The
170 multibeam bathymetry dataset covers the Gippsland Basin continental shelf, at around
171 200 m water depth, to the Tasman Sea Abyssal plain, at over 4000 m water depth
172 (Figure 3A).

173

174 3.2 Seismic data

175 We adopt two types of seismic reflection data provided by Geoscience Australia
176 (<http://www.ga.gov.au/nopims>): (i) A 2D regional seismic section which is up to c. 90

177 km long, therefore providing excellent coverage from Gippsland Basin shelf region to
178 Bass Canyon abyssal plain (Figure 3C); and (ii) two 3D seismic reflection surveys (Elver
179 3D and Tuskfish 3D), which covered an area of c. 650 km² and 1050 km², respectively
180 (Figure 2B). Both 3D seismic datasets are post-stack time-migrated and zero-phase
181 processed, and a downward decrease and increase in acoustic impedance are
182 expressed as blue (negative) and red (positive) seismic reflections, respectively. The
183 3D seismic surveys have a dominant frequency content of 70 hertz and an average
184 seismic velocity of 1700 m/s near the seabed sediment, which gives an approximate
185 vertical resolution of c. 6 m for the near seabed sediments. The 3D seismic resolution
186 is therefore sufficient to map the geometry of detailed seabed sedimentary and
187 structural features. We further extract the dip illumination seismic attribute (see
188 Appendix S1 for an explanation), from the 3D seismic dataset to determine the seabed
189 geometries and geomorphology of the interpreted submarine deposits.

190

191 3.3 Piston Core and grain Size

192 Comprehensive sediment sampling and piston cores collection was conducted from
193 RV Franklin cruise in 1998 (FR11/98) (Exon et al., 2002). In this study, we adopted six-
194 piston cores in the continental shelf and slope areas over a water depth range of 200-
195 2500 m. The detailed core descriptions and interpretations are compiled from
196 (Mitchell et al., 2007b), which have provided lithological and sedimentary facies
197 constraints for the study area. In addition, we analyzed seabed grain size distribution
198 data from 13 locations, obtained from the Geoscience Australia Marine Sediment

199 Database (<https://portal.ga.gov.au>). For the purpose of this current research, we
200 analyzed the proportion of mud (<65 μm), sand (between 65 μm and 2 mm) and gravel
201 (> 2mm) within each sampling locations.

202

203 3.4 Sediment incipient motion calculation

204 To determine whether BCC can entrain and suspend sediments during transportation,
205 we calculate the critical condition for sediment incipient motion using the method
206 proposed by Soulsby (1997). Soulsby (1997) equations resolve critical seabed shear
207 stress (τ_{cr}) and bottom shear stress due to currents (τ_b), if $\tau_b < \tau_{cr}$, the seabed
208 sediments are immobile (i.e. no movement), if $\tau_b > \tau_{cr}$, the seabed sediments move
209 and could be suspended and transported (Soulsby, 1997). In continental shelf settings,
210 Soulsby (1997) method is widely applied and has been proved effective for quantifying
211 the threshold of sediment motion under marine current environments (i.e. Villaceros-
212 Robineau et al., 2019).

213

214 The τ_{cr} of seabed composed mainly of cohesive sediments was calculated using
215 Equations (1) - (3) from Soulsby (1997).

$$216 \quad \tau_{cr} = g\theta_{cr}(\rho_s - \rho_w)d \quad (1)$$

$$217 \quad \theta_{cr} = 0.3 / (1 + 1.2D_*) + 0.055(1 - e^{-0.02D_*}) \quad (2)$$

$$218 \quad D_* = [g(\rho_s - \rho_w) / (\rho_w v^2)]^{1/3} d \quad (3)$$

219 where g is gravitational acceleration, 9.81 m/s^2 ; ρ_s is sediment density, 2,650
220 kg/m^3 ; ρ_w is current density of BCC, 1,023.2 kg/m^3 according to Tomczak (1987); d

221 is sediment grain size, ranging from 65 μm to 2 mm on the continental shelf of
222 Gippsland Basin (Figure 8D); θ_{cr} is critical Shields parameter; D_* is dimensionless
223 grain size parameter; ν is kinematic viscosity for seawater, $1.212 \times 10^{-6} \text{ m}^2/\text{s}$ at 35
224 salinity and 15 $^\circ\text{C}$ (Luick et al., 1994).

225

226 The bottom shear stress τ_b and the shear velocity u^* impacted by currents are
227 calculated via the law of the wall, using Equations (4) - (5):

$$228 \quad u^* = kU(z) / \text{Ln}(z / z_0) \quad (4)$$

$$229 \quad \tau_b = u^{*2} \rho_w \quad (5)$$

230 where $U(z)$ is the current velocity measured at a depth of z meter above the
231 seabed, we adopt 20 m of z and chose a current speed of 0.5–1.0 m/s as measured
232 by Acoustic Doppler Current Profiler (Luick et al., 1994); k is von Kármán constant,
233 0.40 ± 0.02 (Bailey et al., 2014); z_0 is reference height related to the seabed, for
234 muddy seabed is estimated to be c. 0.2 mm (Soulsby, 1983).

235

236 4. RESULT

237 We divide the Gippsland Basin into Northern, Central, and Southern regions based on
238 geographical position and seabed morphology (Figure 3A, 3B). The continental shelf of
239 the Central region extends seaward for approximately 70 km with an average dip of
240 0.8° then abruptly steepens to 8.8° in the slope (Figure 3C). The water depth of the
241 Central region ranges from 0-500 m on the shelf and from 500-2000 m on the slope
242 (Figure 3A). Below we describe the seabed geomorphology and the major sedimentary

243 environments from the shelf to the slope in the Central region of the Gippsland Basin.

244

245 4.1 Seabed geomorphology of the shelf area

246 **Observation:** The Central region is characterized by an erosional seabed (Figures 4A,
247 4B). On the shelf, a set of north-trending scallop-shaped scarps have been observed
248 near the outer shelf area (Figure 4C). Seismic sections indicate the scallop-shaped
249 scarps show a clear truncation edge and erosional base surface (termed as basal shear
250 surface), marking the boundary that differentiates the overlying undeformed strata
251 from the deformed sediments (Figures 5A, 5B). Downslope (eastward) to the scarps, a
252 series of sediment wave fields have been observed along the middle part of the outer
253 shelf (Figure 4B, 4C). Further downslope, the sediment waves are dissected by a set of
254 irregular discontinuous concave-downslope scours that occur at the southwestern
255 part of the shelf (Figures 4B, 4C). In the seismic section, the scours range from 1.2-1.7
256 km in width, 1.7-3.4 km in length (spacing), from 80-200 m in depth, and with an
257 aspect ratio (wavelength/height) from 167-221 (Figure 5C). These scours are normally
258 characterized by truncated, steep lee sides and gentle, slightly upslope-dipping stoss
259 sides (Figure 5C). Buried step-like bedforms are observed beneath seabed scours (see
260 insert figure in Figure 5C). The buried bedforms contain sub-parallel, relatively high-
261 amplitude seismic reflections, and show upslope migration by erosion in the lee side
262 and deposition in the stoss side (Figure 5C).

263

264 Further NE, three sets of scours aligned in distinctive or discontinuous channel-shaped

265 depressions have been observed in the centre part of the shelf (Figure 4C). The crests
266 of these scours are consistently oriented approximately north-south, being confined
267 in the axis of channel-shaped morphology (Figure 4C). Seismic sections cutting along
268 the thalweg of the channel-shaped depressions show a series of bedforms that form a
269 train of steps and stretch over a distance of 10-16 km (Figures 5D, 5E). These bedforms
270 range from 0.2-0.7 km in width, 0.9-1.2 km in wave length, 20-60 m in wave height,
271 and with aspect ratio from 46-167 (Figures 5D, 5E). A single bedform is characterized
272 by a steep scarp indicated by truncated seismic reflections that form the lee side
273 contrast with a gently, lower relief slope at the stoss side (Figures 5D, 5E).

274

275 Further NE of the shelf, at least two well-developed channels have been observed in
276 the eastern part of the shelf (Figure 4C). Nevertheless, these channels only extend to
277 the shelf break, and no clear erosions have been observed within the slope (Figures
278 4B, 4C). These channels vary from 2–10 km in width, and 100–325 m in depth (Figure
279 4B). They initially trend SSE and then sharply divert to the NE within a few kilometres
280 distance across the shelf break, and ultimately run to the slope after passing through
281 the shelf break (Figures 4B, 4C). A set of longitudinal lineations has been observed on
282 the southern flank of the channels (Figure 4C). These lineations are c. 8 km long, they
283 are evenly spaced and predominantly oriented parallel to the channel axis. In the
284 seismic section, the longitudinal lineations show a stair-shaped cross-sectional
285 geometry and truncations (Figure 5F).

286

287 **Interpretation:** The scalloped scarps developed near the outer shelf indicate a gradual
288 broadening over time is likely caused by slope failures (i.e. Lee and Chough, 2001). The
289 scalloped scarps are thus interpreted as headwall scarps associated with a buried
290 landslide (Figures 5A, 5B). The scours, scour trains, and channels are developed above
291 the landslide's basal shear surface, suggesting the landslide is being deposited and
292 predate these bedforms (Figures 5C-F). The sediment wave fields developed within the
293 scarps are evident in the presence of downslope currents (i.e. Fildani et al., 2006). The
294 asymmetrical cross-sectional geometry, large aspect ratio, and upslope migration
295 trend indicate the scours are erosional cyclic steps (or cyclic scours) that are carved by
296 downslope flowing supercritical currents (Figure 5C; Fildani et al., 2006; Kostic, 2011).
297 Scours aligned within the channel template are interpreted as erosional cyclic step
298 trains, which may indicate an incipient channel formation (i.e. Taki and Parker, 2005;
299 Fildani et al., 2006; Fildani et al., 2013; Zhong et al., 2015). The buried step-like
300 bedforms are interpreted as partially depositional cyclic steps, formed when sediment
301 erosion on the lee side is less than sediment deposition on the stoss side (Slootman
302 and Cartigny, 2020). The presence of the partially depositional cyclic steps suggests
303 that the downslope flowing currents were active in the Central region for an extended
304 period of time.

305

306 The channel's diversion near the shelf edge could be a result of the Westerly wind-
307 induced Ekman transport flow (ETF), which follows a NE-NNE direction, interacting
308 with the sedimentary systems along the edge of the continental shelf (Mitchell et al.,

309 2007a). The EAC is less likely to contribute to the deviation of the channel axis, as it
310 separates from the coast approximately between 30°S and 32°S, splitting into eddy-
311 dominated southern and eastern extensions (Cetina-Heredia et al., 2014; Oke et al.,
312 2019). The major eddies are anticlockwise, and therefore, the channel courses should
313 be diverted to the southeast direction, which is opposite to our observation.

314

315 The longitudinal lineations developed within the channels are interpreted as
316 sedimentary furrows similar to those observed in other submarine settings (i.e. Wynn
317 and Stow, 2002; Puig et al., 2008). Studies of furrows show that these features were
318 formed due to recurring, stable, and directional currents (i.e. turbidity currents)
319 erosion through time (e.g. Flood, 1983; Puig et al., 2008). The presence of furrows in
320 this study suggests that the ambient downslope flowing currents may have strong and
321 persistent energy (Flood, 1983). The sole appearance of furrows on the channel's
322 southern flank suggests that the downslope flowing currents preferential arrival across
323 the southern channel flank.

324

325 4.2 Seabed geomorphology of the slope area

326 **Observation:** Near the upper slope, gullies and landslide scarps are widely distributed
327 on the slope between water depths 700 to 2000 m (Figure 6). The gullies extend
328 several kilometres from the upper slope to the lower slope, terminating as the slope
329 angle decreases and intersects with the Bass Canyon head (Figures 4B, 6). The gullies
330 are straight and oriented to the dip direction of the slope, characterized by linear

331 morphology, rounded heads and narrow bodies in plain view (Figure 6). Small failures
332 and slide scarps are evident within or around the edges of the gullies. In the seismic
333 section, these gullies are V-shaped, and have a relatively flat base reflection with clear
334 erosive truncation along the sidewalls (Figure 7A). The gully sidewalls have a relief
335 (incision depth) of 110-230 m, and a width of 120-280 m (Figure 7A). The landslide
336 scarps roughly dip from NNE to SSW, with widths ranging from c. 4 km to 7km (Figure
337 6). In seismic sections, these scarps show a stair-shape, backward (i.e. landward)
338 dipping geometry (Figure 7B).

339

340 Near the lower slope, scours that are aligned in train and parallel to the slope dip
341 direction have been observed within the gullies and on the inter-gully ridges (Figure
342 6). Seismic sections cutting along the thalweg of the scour trains show that they are
343 characterized by steep and erosional lee sides and gentle stoss sides, similar to the
344 cyclic steps developed on the shelf (Figures 7B-D). These scours are 0.5-1.3 km in
345 wavelength, 9-19 m in wave height, and aspect ratio is from 12-40. They are best
346 developed near the lower slope, where the slope gradient drops from 9° - 12° (near the
347 upper slope) to 4° - 7° (to the lower slope; Figures 7B-D). Further lower slope, giant
348 landslide scarps that distribute more than 30 km horizontally are observed near the
349 lowermost of the slope (Figure 6). In the seismic section, the scarps show clear
350 truncations that separate the undeformed seabed (upslope) from the deformed
351 erosional seabed (downslope) (Figures 7B-D).

352

353 **Interpretation:** Near the upper slope, the step-shaped pattern of the scarps suggests
354 a retrogressive failure mechanism of the landslides (Figure 7B; Wu et al., 2021). As the
355 landslide is located along the shelf edge, where cyclic wave loading can constantly
356 rework seabed sediments. This process may account for a potential trigger mechanism
357 leading to slope failure (i.e. Marshall et al., 1978; Bea et al., 1983). The gullies clearly
358 incise into the landslides, suggesting that they post-date the slope failures (Figure 6).
359 The linear gullies are interpreted as the conduits for gravity flows to transport
360 sediment to deeper waters (Micallef and Mountjoy, 2011; Lonergan et al., 2013). The
361 V-shaped head geometry indicates the origin of the gullies is associated with
362 downslope gravity-driven currents (i.e. debris flow and turbidity current; Farre et al.,
363 1983; Gales et al., 2012). Successive small failures are exhibited on the gully ridges,
364 which is indicative of a gradual widening of the gullies (Post et al., 2022). The scour
365 trains developed within the gullies and on the inter-gully ridges are interpreted as
366 cyclic steps, similar to their counterparts developed on the shelf (i.e. Fildani et al.,
367 2006). The presence of cyclic steps suggests that the slope area is also a supercritical
368 flow regime-dominated environment, and the erosion by supercritical currents might
369 play a role in the gully's initiation and evolution (i.e. Noormets et al., 2009; Gales et al.,
370 2012).

371

372 Our observation suggests that cyclic steps are scarce on the upper slope, where the
373 slope gradient is steeper (9° - 12°), but prominent on the lower slope, where the slope
374 gradient is relatively gentle (4° - 7°) (Figures 7B-D). The discrepancy of the cyclic steps

375 on the upper slope can be explained as the higher slope gradient can cause the
376 overflowing currents to have a faster velocity, thereby suppressing their ability to
377 decelerate and undergo internal hydraulic jumps (Kostic, 2011; Zhong et al., 2015). Due
378 to the higher flow velocity (therefore more energetic), erosional scours and
379 truncations are common on the upper slope (Figures 7C, 7D). Further downslope,
380 cyclic steps preferentially form near the lower slope area (Figures 7B-D), suggesting
381 the transition from high slope gradients to low slope gradients could promote the
382 formation of the cyclic steps (i.e. Covault et al., 2017; Fildani et al., 2021). The
383 construction of cyclic steps has led to the formation of local high topographies near
384 the distal side of the lower slope (Figures 7B-D). These local topographic highs can
385 form 12°-22° slopes and range from 70-130 m high, leaving a series of spatially
386 evacuated accommodations near the distal edge of the lower slope (Figures 7B-D).
387 These evacuated accommodations can reduce the lower slope's lateral confining
388 pressure, thus increasing seabed instability (Bull et al., 2009). This can be evidenced
389 by the giant submarine landslides occurring immediately adjacent to, and continuous
390 headwall scarps developing near the distal side of the local topographic highs (Figures
391 7B-D). Therefore, we indicate that the local topographic highs can act as landslide-
392 susceptible structures that ultimately prime slope failures.

393

394 4.3 Piston core and grain size analysis

395 **Observation:** Facies-1 can be observed from the shelf and slope (core #1-4 and 6;
396 Figure 4B). On the shelf, Facies-1 are observed within the headwall scarps of the buried

397 submarine landslide (Figure 4B). Facies-1 is normally graded, moderately to well-
398 sorted, and contains coarse-grained sand (predominately near the lower part) with a
399 sharp top surface and an erosional base surface (Figure 8A). Facies-1 collected from
400 the slope area suggests this facies is internally structureless and contains shelf-
401 restricted bioclasts (core #4 and 6; Figure 4B). Facies-2 can be observed from the
402 upper-lower slope (core #5 and 6; Figure 4B). Facies-2 contains sand- and silt-sized
403 bioclasts, quartz and siliciclastic clay. Core observation indicates it is poorly sorted,
404 matrix-supported and often organic-rich (Figure 8B). It also has decimetre-thick
405 bedding with gradational contacts with bioturbation observed (Figure 8B).

406

407 There are significant differences in grain size distributions between sediment samples
408 collected outside (west) and within (east) the headwall scarps associated with the
409 buried landslide (Figure 8C). Sediment samples collected upslope (west) of the
410 headwall scarps show fine-to-medium sand grain size, and the predominant particle
411 diameter is between 65 μm and 2 mm (Figure 8C). In comparison, sediment sample
412 collected within the headwall scarps exhibits sharp grain size variations (Figure 8C).
413 Specifically, the sediment has an average particle diameter exceeding 2 mm and
414 consists primarily of coarse-grained gravel.

415

416 **Interpretation:** The erosional base surface, coarse-grained, normally graded, and
417 internally structureless nature of Facies-1 is a typical indicator of Bouma Ta-typed
418 turbidites, which are primarily formed by down slope transported turbidity currents

419 (Bouma, 1962). The abundance of shelf-restricted bioclasts observed from the slope
420 suggests these turbidites originated from the shelf. Therefore, we interpret Facies-1 as
421 turbidites formed by turbidity currents sourced from the continental shelf. The fine-
422 grained and organic-rich nature of Facies-2 suggests it is deposited under a low energy
423 condition. We interpret Facies-2 as representing the background slope environment
424 (Mitchell et al., 2007b).

425

426 BCC is the dominant oceanographic process on the shelf of the central Gippsland Basin
427 (Mitchell et al., 2007b), considering the minimum (c. 0.5 m/s) and maximum (c. 1.0
428 m/s) speed of the BCC (Luick et al., 1994), the sediment grain size that is smaller than
429 $639 \mu\text{m}$ and 2.036 mm would be motional, respectively (Figure 8D). The BCC is
430 therefore capable of entraining most sediment calibres from the seabed (Figure 8C)
431 and of forming dense, bottom nepheloid layers during transportation, as suggested by
432 previous monitoring studies (i.e. Godfrey et al., 1986). The sudden increase in grain
433 size collected within the headwall scarps suggests a highly turbulent and energetic
434 flow that is capable of carrying coarse-grained sediments is active (Postma and
435 Cartigny, 2014). Core analyses conducted in the same area indicate this highly
436 turbulent and energetic flow is downslope transported turbidity current. Thus, the
437 significant change in grain size may be attributed to the transition from along-shelf
438 transported BCC to downslope transported turbidity current, and the transformation
439 process occurs adjacent to the headwall scarps of the buried landslide.

440 5. DISCUSSION

441 5.1 Turbidity current: the dominant sedimentary process in central 442 Gippsland Basin

443 The seismic interpretations reveal a continued presence of cyclic steps throughout the
444 outer shelf and slope areas (Figures 4C and 6), which indicate a continuing role of
445 downslope-transported supercritical currents in sculpting and remoulding the seabed
446 in the central Gippsland Basin (i.e. Fildani et al., 2006; Kostic, 2011; Zhong et al., 2015).

447 Published studies suggest that the overriding flow that creates cyclic steps is
448 supercritical currents with alternating transformation between supercritical and
449 subcritical flow through hydraulic jumps (i.e. Zhong et al., 2015; Covault et al., 2017;
450 Fildani et al., 2021). Core observation and grain size analyses have confirmed this
451 interpretation, as coarse-grained, Ta-typed turbidites are the major facies, indicating
452 the presence of high-intensity downslope-traversing turbidity currents (Figures 8A, 8C;
453 Bouma, 1962). Additionally, recent publications indicate that Ta-typed turbidites can
454 be formed by hydraulic jump-related rapid sedimentation, often associated with high-
455 energy supercritical turbidity currents (Figure 8A; i.e. Postma and Cartigny, 2014).
456 Therefore, by combining the results from seismic interpretation, core observation, and
457 grain size analyses, we interpret that turbidity currents are an important sedimentary
458 process in the central Gippsland Basin.

459

460 5.2 The initiation of turbidity current: transformation from the dense shelf 461 water cascade

462 The origin of turbidity currents has been attributed to three main processes,
463 transformation from the slope failures, hyperpycnal flows from onshore fluvial input
464 or subglacial meltwater, and oceanographic processes generated flows near the
465 shelf edge (Piper and Normark, 2009; Talling et al., 2013). In Gippsland Basin, the
466 Central region has been completely disconnected from onshore drainage systems
467 since the Pliocene (Mitchell et al., 2007b), and no modern submarine landslides (only
468 buried landslide; Figure 5B) are observed in the central shelf. Therefore, slope failures
469 and onshore fluvial input cannot contribute to the initiation of turbidity currents.
470 Oceanographic processes including storms, tides, and internal waves may play a role
471 in resuspending seabed sediments and igniting episodic flows. Nevertheless, as they
472 occur periodically in most circumstances and their influence is often multi-directional,
473 they thus lack the ability to generate recurring and stable currents. This contrasts with
474 our observations, where the erosional features developed on the shelf are inferred to
475 reflect a recurring, directionally stable flow that is sufficiently strong to erode the
476 seabed (i.e. Figures 4C, 5C-F). BCC is the primary oceanographic process active on the
477 shelf of the Central Gippsland Basin (Mitchell et al., 2007b), and it could be a
478 reasonable cause of turbidity currents. The following sections will examine the
479 processes involved in this current transformation and examine how turbidity currents
480 can be maintained during transportation.

481

482 As BCC propagates along and cascades across the continental shelf of the Gippsland
483 Basin, the sediment entraining process has allowed a density contrast near the bottom

484 of the BCC from the surrounding seawater, forming dense, bottom nepheloid layers
485 that hover above the seabed (Figures 9A, 9B; Godfrey et al., 1980; Mitchell et al.,
486 2007b). An equilibrium condition could have remained when BCC flows within a
487 relatively smooth and flat (c. 0.8°) shelf region, until it flows into the area affected by
488 the pre-existing landslide. The headwall scarps of the landslide are 40-70 m deep and
489 are characterized by a steep gradient (7°-10°), which has caused local seabed
490 depressions and slope gradient variation (Figures 9B, 9C). When the bottom nepheloid
491 layer moves across and flows over these headwall scarps, a sudden increase in slope
492 gradient could breach the flow equilibrium condition and enhance the shear stress
493 (thus entraining capacity) and flow velocity (Ogston et al., 2008; Traer et al., 2012;
494 Traer et al., 2018). Consequently, the headwall scarps can cause the dense nepheloid
495 layers to split and sink (Figure 9C). The denser layer would subsequently hover over
496 the seabed and potentially accelerate when traversing the scarps (Figure 9C).
497 Accelerating flows could cause additional perturbations and entrain more sediment,
498 and ultimately ignite a turbidity current (Figure 9C; i.e. Parker et al., 1986; Ogston et
499 al., 2008). The headwall scarps on the shelf extend over 70 km along the BCC's
500 transport direction (Figures 3A and 9A), which allows the above-mentioned process to
501 continue and sediments to remain suspended as the BCC moves. As sediments are
502 continuously resuspended, they serve as a recurrent source of turbidity current
503 ignition. Therefore, we summarize on the continental shelf the landslide emplacement
504 first, then cascading water opportunistically uses the headwall scarps as a
505 'perturbation point' to transform into turbidity currents and lock in place for cyclic

506 steps (Figure 9A). Other oscillatory oceanographic processes, including Westerly wind-
507 generated strong wave actions and storm-generated currents, may coincide with the
508 BCC (or act as external forces to enhance the BCC) and simultaneously resuspend large
509 amounts of seabed unconsolidated sediments and generate downslope flows,
510 potentially contributing to the initiation of turbidity currents (Figure 9D; Micallef and
511 Mountjoy, 2011; Talling et al., 2013).

512

513 After ignition, the steep gradient (7° - 10°) of the headwall scarps would provide ample
514 opportunity for turbidity currents to evolve into the Froude supercritical regime
515 (Figure 9C). Piper et al. (1999) demonstrate a similar process in the Grand Banks,
516 where a 6° scarp can facilitate debris flow to transform into supercritical turbidity
517 currents. During transportation, the hydraulic jumps could strengthen flow turbulence
518 by producing large-scale eddies and standing waves within the turbidity current and
519 promote the erosional process (Mulder and Cochonat, 1996; Traer et al., 2012; Hiscott
520 et al., 2013). The presence of 10-16 km-long cyclic step trains suggests that the
521 turbidity currents have high flow intensity and can repeatedly shape the seabed
522 (Figure 4C). Therefore, we indicate that the ignited turbidity currents are unlikely to
523 settle from suspension and have strong energy to transport downslope for a long
524 distance.

525

526 5.3 When and where does this transformation occur?

527 The study area is not the only place where such current transformation occurs, similar

528 diagnostics have been found in the SW Adriatic margin and the NW Mediterranean
529 Seas. The DSWCs in these two places can also entrain seabed sediment and form
530 bottom-dense nepheloid layers, and therefore, potentially initiate turbidity currents
531 (see Appendix 3 for quantification details). In the SW Adriatic margin, where DSWC
532 flows into Gondola Slide's headwall scarp region, the DSWC creates an area of extreme
533 seabed complexity characterised by several large-scale scours aligned in a channel
534 template (cf. Figure 7 of Canals et al., 2009). In the Bari Canyon system, Trincardi et al.
535 (2007) proved that when intense DSWC flows through the canyon head, it can be
536 captured, confined, and transported in a flow regime similar to that of a turbidity
537 current. In the NW Mediterranean Seas, when DSWC cascades into and channelizing
538 through the head of the Cap de Creus Canyon, it carries coarse particles and forms
539 field of giant furrows and overconsolidated the substrate mud (Puig et al., 2008; Puig,
540 2017). Additionally, when DSWC cascades into the canyon heads of the Bourcart
541 Canyon, the current accelerates and transports coarser particles than before entering
542 the canyon head (Gaudin et al., 2006). All the seabed geomorphologies and erosive
543 features identified in the above-mentioned studies require directional, stable and
544 highly energetic processes to develop. Although the published works interpret these
545 erosional features as being formed by the DSWC (Canals et al., 2006; Puig et al., 2008),
546 it is highly reasonable that the DSWC interacted with the pre-existing seabed
547 topographies and transformed into a turbidity current before creating these erosional
548 bedforms. The transformed turbidity current thus carries coarse material and abrades
549 the seabed, induces resuspension and generates erosive bedforms.

550

551 Therefore, we note that the transformation of the DSWC into turbidity currents should
552 be a common process on the outer continental shelves globally. We infer that this
553 current transformation can occur where the seabed gradient has a sharp increase,
554 usually caused by the presence of faults and folds associated with submarine
555 landslides and/or canyons. The newly transformed turbidity currents are competent
556 to establish erosional conditions and become sufficiently large and energetic to carry
557 coarse-grained sediments to reach the lower slope and even the basin floor.
558 Additionally, this current transformation has unravelled the puzzle for the long-
559 distance transportation ability of the DSWC, since turbidity currents can often extend
560 hundreds of kilometres and constitute a significant mechanism for sediment transfer
561 from shallow to deep marine settings (i.e. Pirmez and Imran, 2003).

562

563 5.4 The evolution of seabed geomorphology

564 Cyclic steps and related supercritical bedforms are recognised as fundamentally
565 important building blocks of seabed geomorphology evolution in many submarine
566 settings (Fildani et al., 2006; Covault et al., 2017; Fildani et al., 2021). In the Gippsland
567 Basin, the cyclic steps and cyclic step trains can represent morphodynamic signals for
568 turbidity current channel initiation (cf. Figure 7 of Fildani et al., 2013; Fildani et al.,
569 2021). Under the continuous erosion associated with turbidity currents, these cyclic
570 steps could migrate upslope and focus turbidity currents, gradually coalesce and
571 eventually become a developed channel (Figure 10A, 10B; Fildani et al., 2013). The

572 channel could further evolve laterally and longitudinally, ultimately forming a mature
573 submarine drainage network (i.e. canyon) under the maintenance of sediment capture
574 associated with turbidity currents (Figure 10C). On the slope, the supercritical turbidity
575 currents have resulted in considerable seabed erosion, generating widespread gullies
576 that represent an immature drainage system (Figure 10B; Santangelo et al., 2013).
577 With the continuous downslope transportation of the turbidity currents and other
578 gravity flows (i.e. submarine landslide), the gullies will act as preferential conduits for
579 large-scale sediment transfer and may evolve into canyons (Figure 10C; Santangelo et
580 al., 2013).

581

582 6. Implication

583 6.1 For biodiversity and carbon sequestration

584 The DSWC often occur in late winter to early spring, at a time synchronous with high
585 biological production levels (i.e. marine phytoplankton bloom), the DSWC can thus
586 efficiently transfer significant quantities of minerals, organic material and oxygen,
587 supplying the functioning of continental shelf ecosystems (Sanchez-Vidal et al., 2008).

588 The transformation from DSWC to turbidity current could act as a fast way of fuelling
589 and renewing nutrients from the shallow marine to the deeper marine environment
590 (i.e. water depth > 1000 m). This process could significantly enhance biodiversity in the
591 slope and abyssal environment (Danovaro et al., 2009; Harris, 2014). On the other
592 hand, the cascading current can carry huge amounts of organic carbon and store them
593 in the shallow marine (Canals et al., 2006). The subsequent transformation to turbidity

594 current allows the shallowly stored organic carbon to travel to deeper marine and thus
595 contribute to submarine carbon sequestration as deeper marine has higher reservoir
596 potential and carbon is less likely to return to the atmosphere. Therefore, the current
597 transformation mechanism presented in this study contributes to the ventilation of
598 intermediate and deep waters in the oceans and has a significant impact on
599 biogeochemical cycles and carbon sequestration.

600

601 6.2 For natural hazard mitigation

602 The emplacement of turbidity currents could break valuable seabed
603 telecommunications cables that carry >95% of global data (Carter et al., 2014) and
604 damage submarine pipelines may cause potential hydrocarbon leakage hazards
605 (Porcile et al., 2020). In 2022, the Australian Government announced new wind farm
606 construction plans on the Victorian Coast in the Gippsland Basin (the same area as this
607 study; see from Victorian State Government website). Therefore, we suggest that
608 future marine spatial planning and offshore constructions should consider a
609 reasonable band of the buffer zone (e.g. 10-20 km wide; Figure 10C) landward to the
610 landslide headwall scarps located in the central shelf. We also indicate that new
611 geological and geophysical datasets (including sedimentary cores, additional 3D
612 seismic reflection data, crewed submersible dives, and Autonomous Underwater
613 Vehicles) need to assess modern seabed conditions (oceanographic and
614 geomorphology), to provide better suggestions for future assessments.

615

616 7. CONCLUSION

617 Our results elucidate the dense shelf water cascade (DSWC) can interact with pre-
618 existing submarine landslides and subsequently transform into (supercritical) turbidity
619 currents. The newly transformed turbidity currents are an effective seabed sculpting
620 tool and hugely influenced the modern seabed geomorphology and sedimentation
621 process. We infer that this current transformation can occur where the seabed
622 gradient has a sharp increase, usually caused by the presence of faults and folds
623 associated with submarine landslides and/or canyons. As DSWC is prominent on many
624 continental margins, we suggest that this current transformation represents an
625 unappreciated, yet important trigger for turbidity currents on the outer continental
626 shelves globally.

627

628 ACKNOWLEDGMENTS

629 We thank Prof. Jean-Philippe Avouac for handling our manuscript, and we thank Dr
630 Andrea Fildani for his constructive comments that have greatly improved the
631 manuscript. We thank Geoscience Australia for providing seismic reflection,
632 multibeam bathymetry, and grain size data for the Gippsland Basin and Bass Canyon.
633 Seismic reflection, multibeam bathymetry and grain size data are available from the
634 Geoscience Australia Data Portal: <https://portal.ga.gov.au/persona/marine>. We thank
635 Dr Yulong Zhao for the helpful discussion on the quantification of sediment incipient
636 motion, and we thank Dr Xingxing Wang, Dr Wei Li, and Dr Yongpeng Qin for their
637 helpful discussions during the manuscript preparation. The first author thanks the

638 Fundamental Research Funds for the Central Universities, the Natural Science
639 Foundation of Shanghai (under Grant No. 23ZR1467800), the Shanghai Sailing Program
640 (under Grant No. 22YF1450100) and State Key Laboratory of Marine Geology (under
641 Grant No. MGZ202303) for their financial support.

642 **FIGURE CAPTIONS**

643 Figure 1. (A) Occurrence previously documented dense shelf water cascade (DSWC)
644 around the world. Numbers in each area refer to the location: (1) Eastern Chukchi Sea
645 shelf, (2) Beaufort Sea shelf, (3) Foxe Basin, northernmost part of Hudson Bay, (4) SW
646 Greenland margin, (5) Northern gulf of California, (6) North American south-eastern
647 shelf, (7) Great Bahama Bank, (8) East Greenland Shelf and south of Denmark Strait,
648 (9) West Spitsbergen shelf, (10) Bear Island Channel, Barents Sea, (11) hindered in
649 Storfjord, Barents Sea, (12) Skagerrak, eastern flank of the North Sea, (13) Rockall Bank,
650 North Atlantic Ocean, (14) Celtic Sea shelf, North Atlantic Ocean, (15) Gulf of Lion, NW
651 Mediterranean Sea, (16) Gondola slide area, Adriatic Sea shelf, (17) Cape Bari, SE
652 Adriatic Sea shelf, (18) Southern Mediterranean Sea shelf, (19) Aegean Sea shelf, (20)
653 Banc d'Arguin, near Cape Blanc and off the west African coast, (21) Western shelf of
654 Novaya Zemlya, Barents Sea, (22) shelf of Nansen Basin, Arctic Ocean, (23) North-
655 eastern Severnaya Zemlya shelf, Laptev Sea, (24) Northern sea of Okhotsk, north-
656 western Pacific Ocean, (25) Peter the Great Bay, near the Japan Sea continental slope,
657 (26) NW Australia inner shelf, (27) Shark Bay, western Australia, (28) Great Australian
658 Bight, southern Australia, (29) Jervis Bay, southern Australia, (30) Bass Strait, south-
659 eastern Australia, (31) Spencer Gulf, east Australia, (32) The Hikurangi subduction
660 margin, SE of central New Zealand, (33) The western Ross Sea, Antarctic Ocean, (34)
661 The Adélie Coast, East Antarctic sector, Antarctic Ocean, (35) Prydz Bay, East Antarctica,
662 (36) Southern margin of Weddell Sea shelf, (37) Eastern margin of Weddell Sea shelf,
663 (38) The southern Ross Sea, Antarctic Ocean. Note that the blue dots are based on the

664 DSWC global atlas by Ivanov et al. (2004) and the DSWC recorded around Australian
665 shelves by Mahjabin et al. (2020). The pink dots indicate recently reported (2004–
666 present) cascading phenomena measured by long-term and high-frequency in situ
667 measurements globally, see Appendix 2 for the supporting references. (B) Schematics
668 of the DSWC mechanism showing the formation of intermediate nepheloid layers on
669 the shelf and the downslope turbidity currents. Adapted from Fohrmann et al. (1998).
670

671 Figure 2. (A) The regional map of Australia shows the location of the study area
672 (indicated in a red polygon) and the oceanographic setting. The trajectories of the main
673 oceanic currents are represented by white, blue, and yellow dashed lines. LC, Leeuwin
674 Current; SAC, South Australian Current; ZC, Zeehan Current; BCC, Bass Cascade Current;
675 EAC, East Australian Current. In Gippsland Basin, when the BCC flows through the Bass
676 Strait during winter, it is further fed by the LC, ZC and the wind stress within the Bass
677 Strait, jointly transporting Bass Strait water towards the front (Li et al., 2005; Mitchell
678 et al., 2007b). During summer, though the BCC is less active, strong offshore wind and
679 tidal activities can further reinforce and transport Bass Strait water eastwards (Godfrey
680 et al., 1980). (B) Zoom in view of the Gippsland Basin and the Bass Canyon. Note the
681 north arrow (white) and the yellow box denote the location of the 3D seismic data.
682 The transportation pathway of the BCC is based on data collected from the
683 Conductivity, Temperature, and Depth (CTD) sensors adopted during the winter of
684 1981 by Tomczak (1985). The transportation pathway of the EAC is adopted from
685 Lavering (1994) and Ridgway and Hill (2009). (C) Temperature profile of the Bass Strait

686 showing the downward temperature anomalies within the continental shelf and slope.

687 (D) Temperature profile (potential temperature) in offshore eastern Australia, showing

688 the depth of the East Australian Current (EAC). The temperature data is from the WOCE

689 (World Ocean Current Experiment) Hydrographic Program (available at

690 <https://odv.awi.de/data/ocean>). See Figure 2A for locations.

691

692 Figure 3. (A) 3D view of seabed multibeam bathymetric map of the offshore Gippsland

693 Basin and Bass Canyon system, showing the main geomorphologic features. (B) Sketch

694 of Figure 3A, showing the key depositional elements, canyons and distinguished

695 regional domains. (C) Shelf-to-slope seismic profile showing the Central shelf and slope

696 regions. See Figure 3B for location.

697

698 Figure 4. (A) Seabed structure map generated from the 3D seismic data, showing the

699 seabed morphology in the Central Region. (B) Dip illumination attribute map

700 calculated from the 3D seismic data, showing the detailed sedimentary structures of

701 the Central Region. Note the yellow dots indicate the piston core location. (C) Zoomed-

702 in view of the continental shelf in the Central Region, emphasizing the sediment waves,

703 cyclic steps and channels. See Figure 4B for location.

704

705 Figure 5. (A) Seismic dip section cut through the headwall scarps of the landslide. (B)

706 Seismic longitudinal profile along the axis of the cyclic step train. (C) Seismic

707 longitudinal profile cutting through the axis of channel-formed cyclic steps. The

708 inserted schematic map shows a series of idealized asymmetrical cyclic steps and
709 hypothetical densiometric Froude number (Fr) variability. Within a single bedform, the
710 supercritical flow creates a hydraulic jump ($Fr > 1$) at the base of the lee side and
711 transfers to subcritical flow ($Fr < 1$) at the stoss side. Subsequently, the subcritical flow
712 reaccelerates to supercritical flow again down to the lee side of the next bedform. The
713 schematic map was modified by Cartigny et al. (2011). (D) Seismic longitudinal profile
714 cutting through the axis of channel-formed cyclic steps. (E) Seismic cross-sectional
715 profile cutting through the channels; note the stair-shaped erosional characteristics of
716 furrows developed on the channel sidewalls. See Figure 4C for locations.

717

718 Figure 6. Zoomed-in view of the continental slope in the Central Region, emphasizing
719 the landslides and gullies. See Figure 4B for location.

720

721 Figure 7. (A) Seismic section illustrating gullies' cross-sectional geometries. (B) Seismic
722 dip section cutting along the gully ridge. (C) Seismic dip section cutting along the gully
723 ridge. (D) Seismic dip section cutting within the gully and along its thalweg. See Figure
724 6 for locations.

725

726 Figure 8. (A) Core sketch generated based on piston core report from the central region
727 of the Gippsland Basin, showing the cross-section of the Facies-1. (B) Core sketch
728 generated based on piston core report, showing the cross-section of Facies-2. Core
729 locations in Figure 4B. (C) Grain size distribution in the Central area of the Gippsland

730 Basin. The blue arrow indicates the transport direction of the BCC. (D) The sediment
731 motion threshold curve under the given values of sediment grain size and BCC current
732 speed.

733

734 Figure 9. (A) The 3D view of the Central Region, showing the seabed morphological
735 structures and major current pathways. (B) Schematic 2D plain view of the Central
736 shelf, illustrating the location of headwall scarps, the pathway of the BCC and its
737 associated supercritical turbidity currents. See Figure 9A for location. (C) Schematic
738 cross-section showing the transformation from BCC to turbidity currents. See the text
739 for explanations and Figure 9B for location. (D) Schematic cross-section depicting the
740 combined influence of the Westerly Wind, internal waves, and tide-induced sediment
741 resuspension and turbidity current initiation. See Figure 9A for location.

742

743 Figure 10. Schematic of seabed geomorphology evolution processes in the Central
744 Region of the Gippsland Basin. (A) Shelf: the transformation of the Bass Cascading
745 Current (BCC) into turbidity currents; Slope: the generation of scarps caused by wave
746 activities near the upper slope. (B) Shelf: The formation of the sedimentary structures
747 caused turbidity currents; Slope: The initiation of gullies and the formation of the
748 landslides on the upper slope. (C) Shelf: The evolution from cyclic steps into channels
749 and canyons; Slope: landslide initiation near the lower slope. Note that the buffer zone
750 indicates a stable seabed not influenced by the current transformation process or the
751 ignited turbidity current.

752 REFERENCE

- 753 Bouma, A.H.P.H.K.F.P.S., 1962. Sedimentology of some Flysch deposits : a graphic approach to
754 facies interpretation. Elsevier, Amsterdam
- 755 Boland, F., 1971. Temperature-salinity anomalies at depths between 200m and 800m in the
756 Tasman sea. *Marine and Freshwater Research* 22, 55-62.
- 757 Marshall, N., Stanley, D., Kelling, G., 1978. Large storm-induced sediment slump reopens an
758 unknown Scripps submarine canyon tributary. *Sedimentation in submarine canyons, fans, and
759 trenches: Stroudsburg, Pennsylvania, Hutchinson and Ross*, 73-84.
- 760 Godfrey, J., Jones, I., Maxwell, G., Scott, B., 1980. On the winter cascade from Bass Strait into
761 the Tasman Sea. *Marine and Freshwater Research* 31, 275-286.
- 762 Bea, R.G., Wright, S.G., Sircar, P., Niedoroda, A.W., 1983. Wave-induced slides in south pass
763 block 70, Mississippi Delta. *Journal of Geotechnical Engineering* 109, 619-644.
- 764 Farre, J.A., McGregor, B.A., Ryan, W.B., Robb, J.M., 1983. Breaching the shelfbreak: passage
765 from youthful to mature phase in submarine canyon evolution.
- 766 Flood, R.D., 1983. Classification of sedimentary furrows and a model for furrow initiation and
767 evolution. *Geological Society of America Bulletin* 94, 630-639.
- 768 Soulsby, R.L., 1983. The bottom boundary layer of shelf seas, Elsevier oceanography series.
769 Elsevier, pp. 189-266.
- 770 Tomczak, 1985. The Bass Strait water cascade during winter 1981. *Continental Shelf Research*
771 4, 255-278.
- 772 Godfrey, J., Vaudrey, D., Hahn, S., 1986. Observations of the shelf-edge current south of
773 Australia, winter 1982. *Journal of Physical Oceanography* 16, 668-679.
- 774 Parker, G., Fukushima, Y., Pantin, H.M., 1986. Self-accelerating turbidity currents. *Journal of
775 Fluid Mechanics* 171, 145-181.
- 776 Tomczak, M., 1987. The Bass Strait water cascade during summer 1981–1982. *Continental
777 Shelf Research* 7, 561-572.
- 778 Rahmanian, V., Moore, P., Mudge, W., Spring, D., 1990. Sequence stratigraphy and the habitat
779 of hydrocarbons, Gippsland Basin, Australia. *Geological Society, London, Special Publications*
780 50, 525-544.
- 781 Colwell, J.B., Constantine, A.E., Willcox, J.B., 1993. Regional structure of the Gippsland Basin:
782 interpretation and mapping of a deep seismic data set. Australian Geological Survey
783 Organisation.
- 784 Lavering, I.H., 1994. Marine environments of Southeast Australia (Gippsland Shelf and Bass
785 Strait) and the impact of offshore petroleum exploration and production activity. *Marine
786 georesources & geotechnology* 12, 201-226.
- 787 Luick, J.L., Ka, R., Tomczak, M., 1994. On the formation and spreading of the Bass Strait cascade.
788 *Continental Shelf Research* 14, 385-399.
- 789 Mulder, T., Cochonat, P., 1996. Classification of offshore mass movements. *Journal of
790 Sedimentary research* 66, 43-57.
- 791 Soulsby, R., 1997. Dynamics of marine sands.
- 792 Fohrmann, H., Backhaus, J.O., Blaume, F., Rumohr, J., 1998. Sediments in bottom-arrested
793 gravity plumes: Numerical case studies. *Journal of Physical Oceanography* 28, 2250-2274.
- 794 Hill, P., Exon, N., Keene, J., Smith, S., 1998. The continental margin off east Tasmania and
795 Gippsland: structure and development using new multibeam sonar data. *Exploration
796 Geophysics* 29, 410-419.
- 797 Piper, D.J., Cochonat, P., Morrison, M.L., 1999. The sequence of events around the epicentre
798 of the 1929 Grand Banks earthquake: initiation of debris flows and turbidity current inferred
799 from sidescan sonar. *Sedimentology* 46, 79-97.
- 800 Lee, S., Chough, S., 2001. High-resolution (2–7 kHz) acoustic and geometric characters of

801 submarine creep deposits in the South Korea Plateau, East Sea. *Sedimentology* 48, 629-644.
802 Exon, N., Hill, P., Partridge, A., Chaproniere, G., Keene, J., 2002. Cretaceous volcanogenic and
803 Miocene calcareous strata dredged from the deepwater Gippsland Basin on RV Franklin
804 Research Cruise FR11/98. *Geoscience Australia Record* 7.
805 Wynn, R.B., Stow, D.A., 2002. Recognition and interpretation of deep-water sediment waves-
806 implications for palaeoceanography, hydrocarbon exploration and flow process interpretation
807 (Introduction to special issue). *Marine Geology* 192, 1-3.
808 Pirmez, C., Imran, J., 2003. Reconstruction of turbidity currents in Amazon Channel. *Marine*
809 *and petroleum geology* 20, 823-849.
810 Ivanov, V., Shapiro, G., Huthnance, J., Aleynik, D., Golovin, P., 2004. Cascades of dense water
811 around the world ocean. *Progress in oceanography* 60, 47-98.
812 Li, F., Dyt, C., Griffiths, C., Jenkins, C., Rutherford, M., Chittleborough, J., 2005. Seabed
813 sediment transport and offshore pipeline risks in the Australian southeast. *The APPEA Journal*
814 45, 523-534.
815 Taki, K., Parker, G., 2005. Transportational cyclic steps created by flow over an erodible bed.
816 Part 1. Experiments. *Journal of Hydraulic Research* 43, 488-501.
817 Canals, M., Puig, P., de Madron, X.D., Heussner, S., Palanques, A., Fabres, J., 2006. Flushing
818 submarine canyons. *Nature* 444, 354-357.
819 Fildani, A., Normark, W.R., Kostic, S., Parker, G., 2006. Channel formation by flow stripping:
820 Large-scale scour features along the Monterey East Channel and their relation to sediment
821 waves. *Sedimentology* 53, 1265-1287.
822 Gaudin, M., Berné, S., Jouanneau, J.-M., Palanques, A., Puig, P., Mulder, T., Cirac, P., Rabineau,
823 M., Imbert, P., 2006. Massive sand beds attributed to deposition by dense water cascades in
824 the Bourcart canyon head, Gulf of Lions (northwestern Mediterranean Sea). *Marine Geology*
825 234, 111-128.
826 Middleton, J.F., Bye, J.A., 2007. A review of the shelf-slope circulation along Australia's
827 southern shelves: Cape Leeuwin to Portland. *Progress in Oceanography* 75, 1-41.
828 Mitchell, J., Holdgate, G., Wallace, M., 2007a. Pliocene–Pleistocene history of the Gippsland
829 Basin outer shelf and canyon heads, southeast Australia. *Australian Journal of Earth Sciences*
830 54, 49-64.
831 Mitchell, J., Holdgate, G., Wallace, M., Gallagher, S., 2007b. Marine geology of the Quaternary
832 Bass Canyon system, southeast Australia: a cool-water carbonate system. *Marine geology* 237,
833 71-96.
834 Trincardi, F., Fogliani, F., Verdicchio, G., Asioli, A., Correggiari, A., Minisini, D., Piva, A., Remia, A.,
835 Ridente, D., Taviani, M., 2007. The impact of cascading currents on the Bari Canyon System,
836 SW-Adriatic margin (Central Mediterranean). *Marine Geology* 246, 208-230.
837 Herrmann, M., Estournel, C., Déqué, M., Marsaleix, P., Sevault, F., Somot, S., 2008. Dense water
838 formation in the Gulf of Lions shelf: Impact of atmospheric interannual variability and climate
839 change. *Continental Shelf Research* 28, 2092-2112.
840 Ogston, A.S., Drexler, T.M., Puig, P., 2008. Sediment delivery, resuspension, and transport in
841 two contrasting canyon environments in the southwest Gulf of Lions. *Continental Shelf*
842 *Research* 28, 2000-2016.
843 Puig, P., Palanques, A., Orange, D., Lastras, G., Canals, M., 2008. Dense shelf water cascades
844 and sedimentary furrow formation in the Cap de Creus Canyon, northwestern Mediterranean
845 Sea. *Continental Shelf Research* 28, 2017-2030.
846 Sanchez-Vidal, A., Pasqual, C., Kerhervé, P., Calafat, A., Heussner, S., Palanques, A., Durrieu de
847 Madron, X., Canals, M., Puig, P., 2008. Impact of dense shelf water cascading on the transfer
848 of organic matter to the deep western Mediterranean basin. *Geophysical Research Letters* 35.
849 Bull, S., Cartwright, J., Huuse, M., 2009. A subsurface evacuation model for submarine slope
850 failure. *Basin Research* 21, 433-443.
851 Canals, M., Danovaro, R., Heussner, S., Lykousis, V., Puig, P., Trincardi, F., Calafat, A.M., de

852 Madron, X.D., Palanques, A., Sanchez-Vidal, A., 2009. Cascades in Mediterranean submarine
853 grand canyons. *Oceanography* 22, 26-43.

854 Danovaro, R., Canals, M., Gambi, C., Heussner, S., Lampadariou, N., Vanreusel, A., 2009.
855 Exploring benthic biodiversity patterns and hotspots on European margin slopes.
856 *Oceanography* 22, 16-25.

857 Noormets, R., Dowdeswell, J., Larter, R.D., Cofaigh, C.Ó., Evans, J., 2009. Morphology of the
858 upper continental slope in the Bellingshausen and Amundsen Seas—Implications for
859 sedimentary processes at the shelf edge of West Antarctica. *Marine Geology* 258, 100-114.

860 Piper, D.J., Normark, W.R., 2009. Processes that initiate turbidity currents and their influence
861 on turbidites: a marine geology perspective. *Journal of Sedimentary Research* 79, 347-362.

862 Ridgway, K., Hill, K., 2009. The East Australian Current.

863 Paull, C.K., Ussler III, W., Caress, D.W., Lundsten, E., Covault, J.A., Maier, K.L., Xu, J., Augenstein,
864 S., 2010. Origins of large crescent-shaped bedforms within the axial channel of Monterey
865 Canyon, offshore California. *Geology* 6, 755-774.

866 Cartigny, M.J., Postma, G., Van den Berg, J.H., Mastbergen, D.R., 2011. A comparative study of
867 sediment waves and cyclic steps based on geometries, internal structures and numerical
868 modeling. *Marine Geology* 280, 40-56.

869 Kostic, S., 2011. Modeling of submarine cyclic steps: Controls on their formation, migration,
870 and architecture. *Geosphere* 7, 294-304.

871 Micallef, A., Mountjoy, J.J., 2011. A topographic signature of a hydrodynamic origin for
872 submarine gullies. *Geology* 39, 115-118.

873 Gales, J., Larter, R., Mitchell, N., Hillenbrand, C.D., Østerhus, S., Shoosmith, D., 2012. Southern
874 Weddell Sea shelf edge geomorphology: Implications for gully formation by the overflow of
875 high-salinity water. *Journal of Geophysical Research: Earth Surface* 117.

876 Traer, M., Hilley, G., Fildani, A., McHargue, T., 2012. The sensitivity of turbidity currents to mass
877 and momentum exchanges between these underflows and their surroundings. *Journal of*
878 *Geophysical Research: Earth Surface* 117.

879 Fildani, A., Hubbard, S.M., Covault, J.A., Maier, K.L., Romans, B.W., Traer, M., Rowland, J.C.,
880 2013. Erosion at inception of deep-sea channels. *Marine and Petroleum Geology* 41, 48-61.

881 Hiscott, R.N., Aksu, A.E., Flood, R.D., Kostylev, V., Yaşar, D., 2013. Widespread overspill from a
882 saline density-current channel and its interaction with topography on the south-west Black
883 Sea shelf. *Sedimentology* 60, 1639-1667.

884 Lonergan, L., Jamin, N.H., Jackson, C.A.-L., Johnson, H.D., 2013. U-shaped slope gully systems
885 and sediment waves on the passive margin of Gabon (West Africa). *Marine Geology* 337, 80-
886 97.

887 Santangelo, M., Gioia, D., Cardinali, M., Guzzetti, F., Schiattarella, M., 2013. Interplay between
888 mass movement and fluvial network organization: An example from southern Apennines, Italy.
889 *Geomorphology* 188, 54-67.

890 Talling, P.J., Paull, C.K., Piper, D.J., 2013. How are subaqueous sediment density flows triggered,
891 what is their internal structure and how does it evolve? Direct observations from monitoring
892 of active flows. *Earth-Science Reviews* 125, 244-287.

893 Bailey, S.C., Vallikivi, M., Hultmark, M., Smits, A., 2014. Estimating the value of von Kármán's
894 constant in turbulent pipe flow. *Journal of Fluid Mechanics* 749, 79-98.

895 Carter, L., Gavey, R., Talling, P.J., Liu, J.T., 2014. Insights into submarine geohazards from breaks
896 in subsea telecommunication cables. *Oceanography* 27, 58-67.

897 Cetina-Heredia, P., Roughan, M., Van Sebille, E., Coleman, M., 2014. Long-term trends in the
898 East Australian Current separation latitude and eddy driven transport. *Journal of Geophysical*
899 *Research: Oceans* 119, 4351-4366.

900 Harris, P.T., 2014. Shelf and deep-sea sedimentary environments and physical benthic
901 disturbance regimes: a review and synthesis. *Marine Geology* 353, 169-184.

902 Postma, G., Cartigny, M.J., 2014. Supercritical and subcritical turbidity currents and their

903 deposits—A synthesis. *Geology* 42, 987-990.

904 Talling, P.J., 2014. On the triggers, resulting flow types and frequencies of subaqueous
905 sediment density flows in different settings. *Marine Geology* 352, 155-182.

906 Zhong, G., Cartigny, M.J., Kuang, Z., Wang, L., 2015. Cyclic steps along the South Taiwan Shoal
907 and West Penghu submarine canyons on the northeastern continental slope of the South
908 China Sea. *Bulletin* 127, 804-824.

909 Covault, J.A., Kostic, S., Paull, C.K., Sylvester, Z., Fildani, A., 2017. Cyclic steps and related
910 supercritical bedforms: building blocks of deep-water depositional systems, western North
911 America. *Marine Geology* 393, 4-20.

912 Puig, P., 2017. Dense shelf water cascading and associated bedforms, Atlas of bedforms in the
913 western mediterranean. Springer, pp. 35-40.

914 Amblas, D., Dowdeswell, J., 2018. Physiographic influences on dense shelf-water cascading
915 down the Antarctic continental slope. *Earth-Science Reviews* 185, 887-900.

916 O'Brien, P., Mitchell, C., Nguyen, D., Langford, R., 2018. Mass Transport Complexes on a
917 Cenozoic paleo-shelf edge, Gippsland basin, southeastern Australia. *Marine and Petroleum*
918 *Geology* 98, 783-801.

919 Traer, M., Fildani, A., Fringer, O., McHargue, T., Hilley, G., 2018. Turbidity current dynamics: 2.
920 Simulating flow evolution toward equilibrium in idealized channels. *Journal of Geophysical*
921 *Research: Earth Surface* 123, 520-534.

922 Oke, P.R., Roughan, M., Cetina-Heredia, P., Pilo, G.S., Ridgway, K.R., Rykova, T., Archer, M.R.,
923 Coleman, R.C., Kerry, C.G., Rocha, C., 2019. Revisiting the circulation of the East Australian
924 Current: Its path, separation, and eddy field. *Progress in Oceanography* 176, 102139.

925 Villaceros-Robineau, N., Zúñiga, D., Barreiro-González, B., Alonso-Pérez, F., de la Granda, F.,
926 Froján, M., Collins, C.A., Barton, E.D., Castro, C.G., 2019. Bottom boundary layer and particle
927 dynamics in an upwelling affected continental margin (NW Iberia). *Journal of Geophysical*
928 *Research: Oceans* 124, 9531-9552.

929 Mahjabin, T., Pattiaratchi, C., Hetzel, Y., 2020. Occurrence and seasonal variability of Dense
930 Shelf Water Cascades along Australian continental shelves. *Scientific reports* 10, 1-13.

931 Morrison, A., Hogg, A.M., England, M.H., Spence, P., 2020. Warm Circumpolar Deep Water
932 transport toward Antarctica driven by local dense water export in canyons. *Science advances*
933 6, eaav2516.

934 Porcile, G., Bolla Pittaluga, M., Frascati, A., Sequeiros, O.E., 2020. Typhoon-induced megarips
935 as triggers of turbidity currents offshore tropical river deltas. *Communications Earth &*
936 *Environment* 1, 1-13.

937 Slooman, A., Cartigny, M.J., 2020. Cyclic steps: Review and aggradation-based classification.
938 *Earth-Science Reviews* 201, 102949.

939 Fildani, A., Kostic, S., Covault, J.A., Maier, K.L., Caress, D.W., Paull, C.K., 2021. Exploring a new
940 breadth of cyclic steps on distal submarine fans. *Sedimentology* 68, 1378-1399.

941 Gales, J., Rebesco, M., De Santis, L., Bergamasco, A., Colleoni, F., Kim, S., Accettella, D.,
942 Kovacevic, V., Liu, Y., Olivo, E., 2021. Role of dense shelf water in the development of Antarctic
943 submarine canyon morphology. *Geomorphology* 372, 107453.

944 Wu, N., Nugraha, H.D., Zhong, F.G., Steventon, M., 2021. The role of mass-transport complexes
945 (MTCs) in the initiation and evolution of submarine canyons.

946 Post, A.L., Przeslawski, R., Nanson, R., Siwabessy, J., Smith, D., Kirkendale, L.A., Wilson, N.G.,
947 2022. Modern dynamics, morphology and habitats of slope-confined canyons on the
948 northwest Australian margin. *Marine Geology* 443, 106694.

949

950

Figure 1

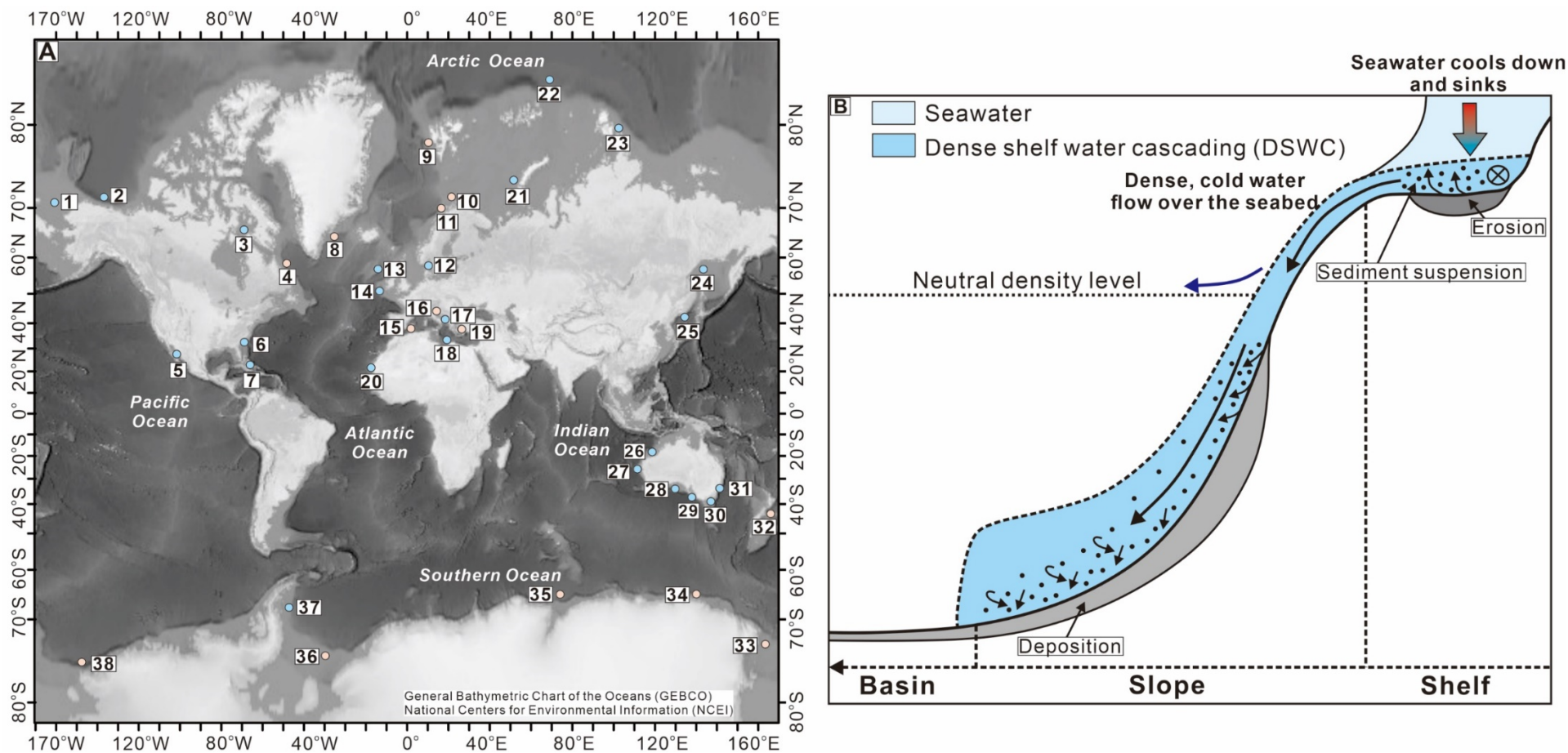


Figure 2

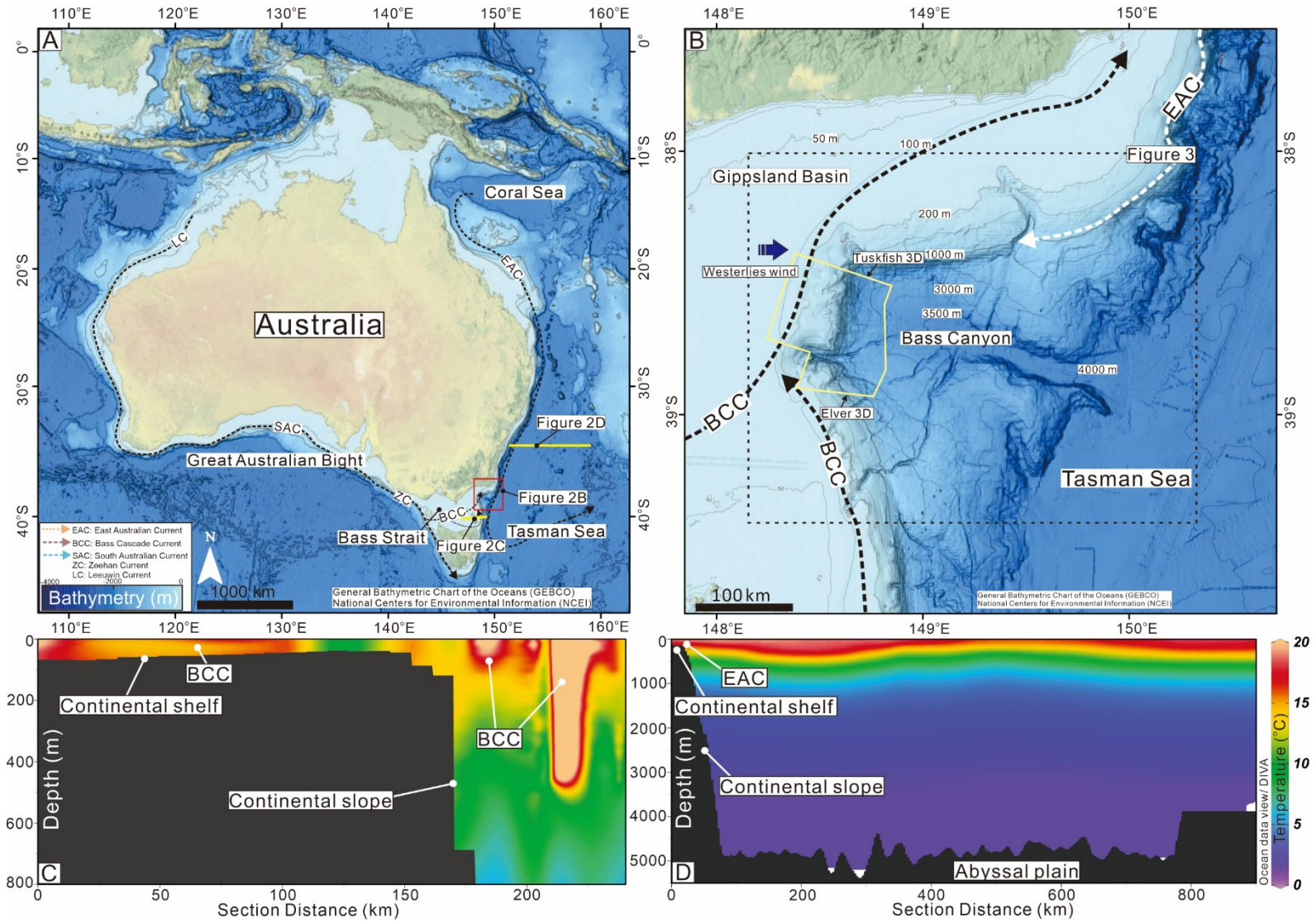


Figure 3

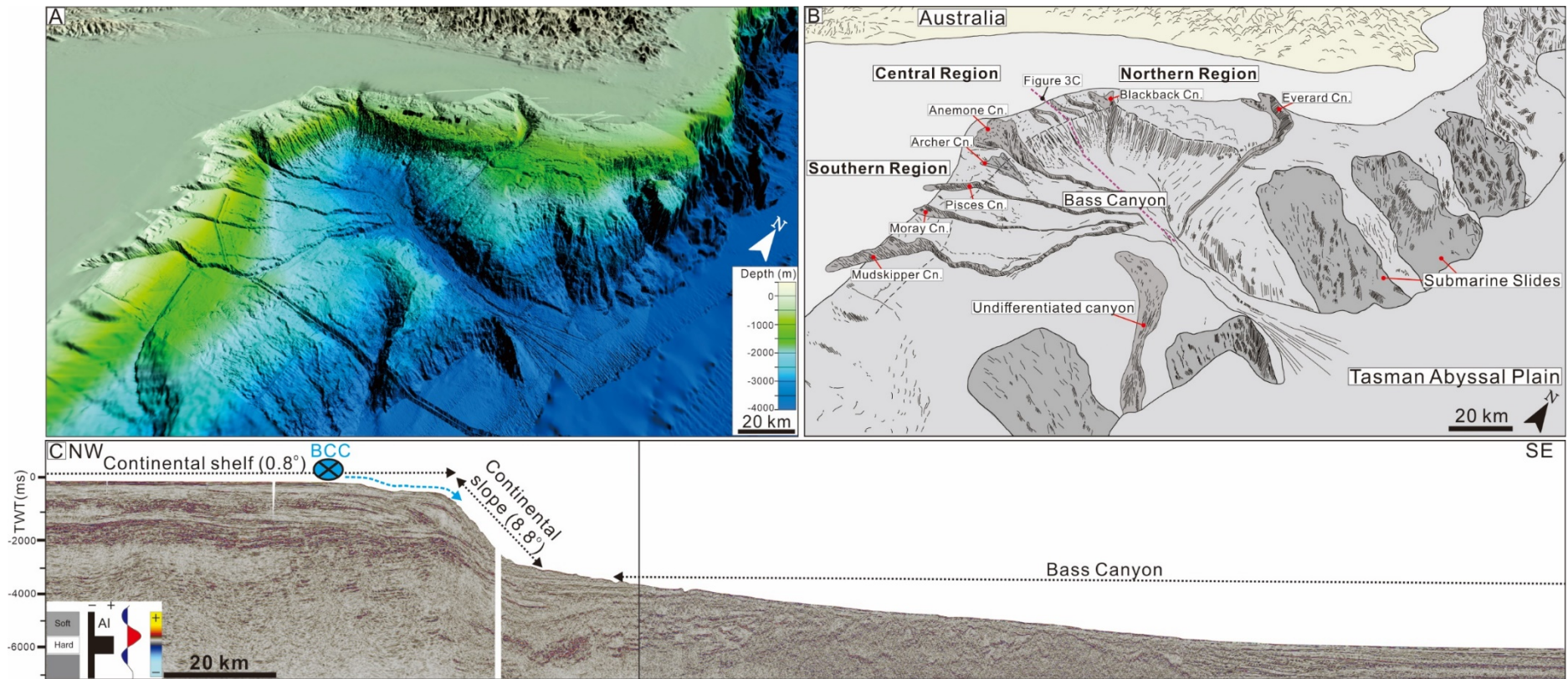
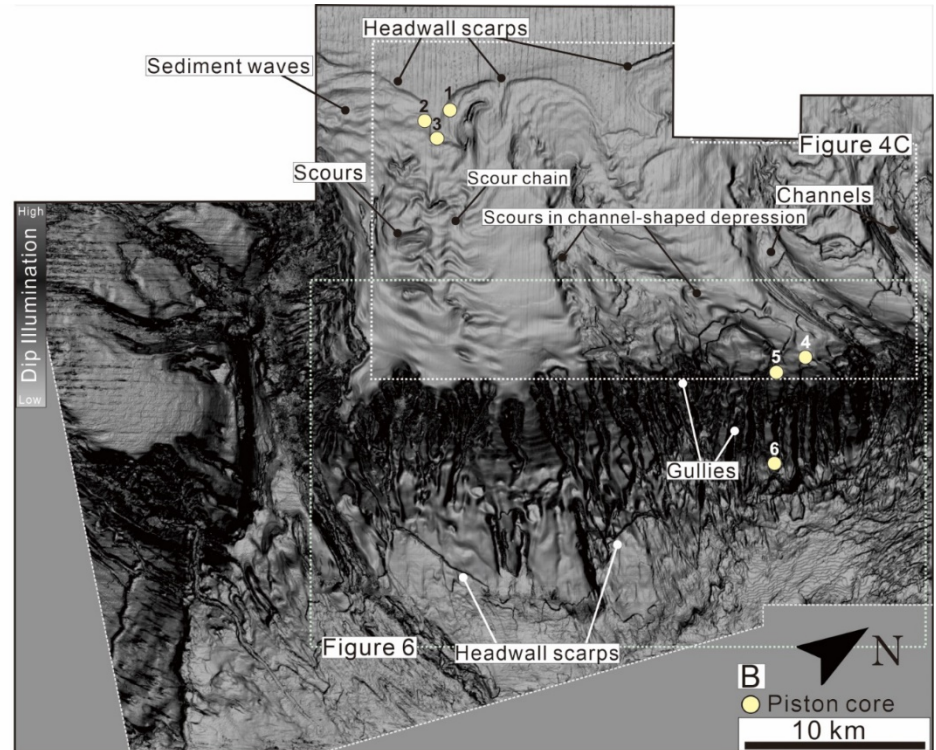
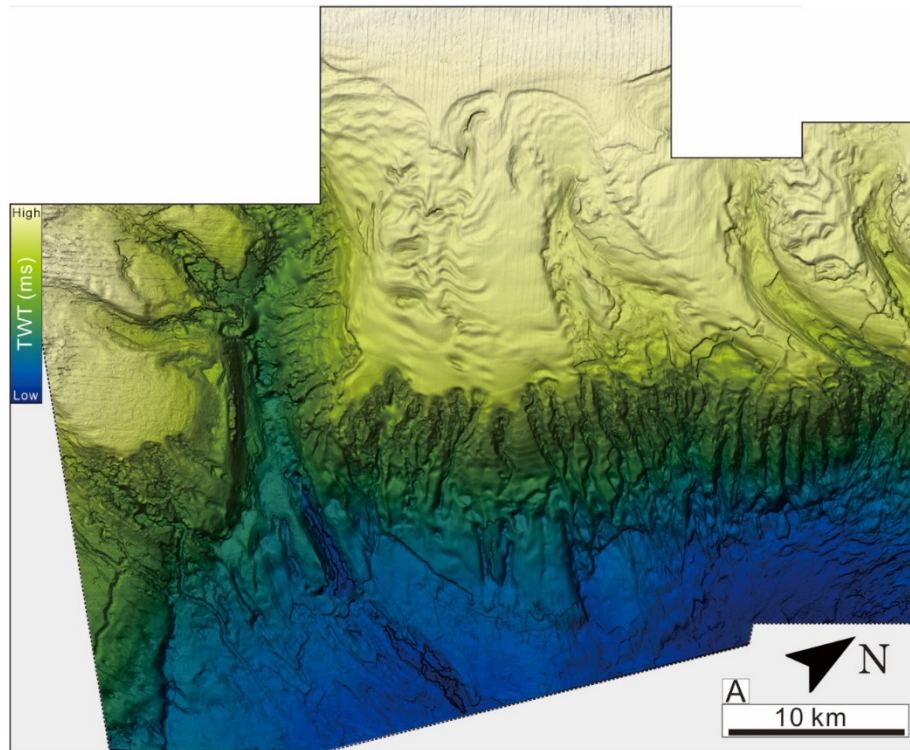
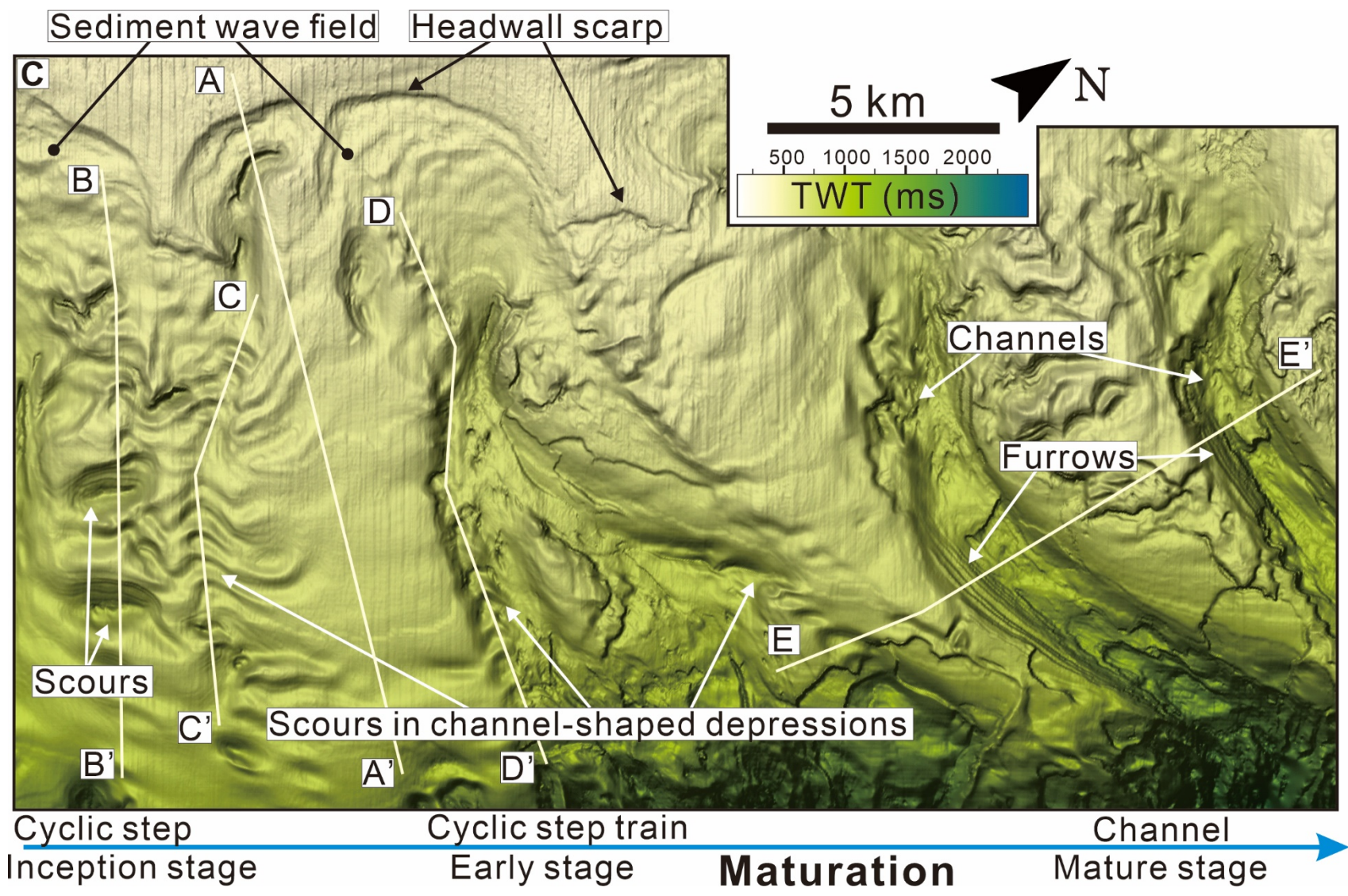


Figure 4





C

A

D

B

C

Channels

E'

Furrows

Scours

E

Scours in channel-shaped depressions

B'

C'

A'

D'

Cyclic step Inception stage

Cyclic step train Early stage

Maturation

Channel Mature stage

Figure 5

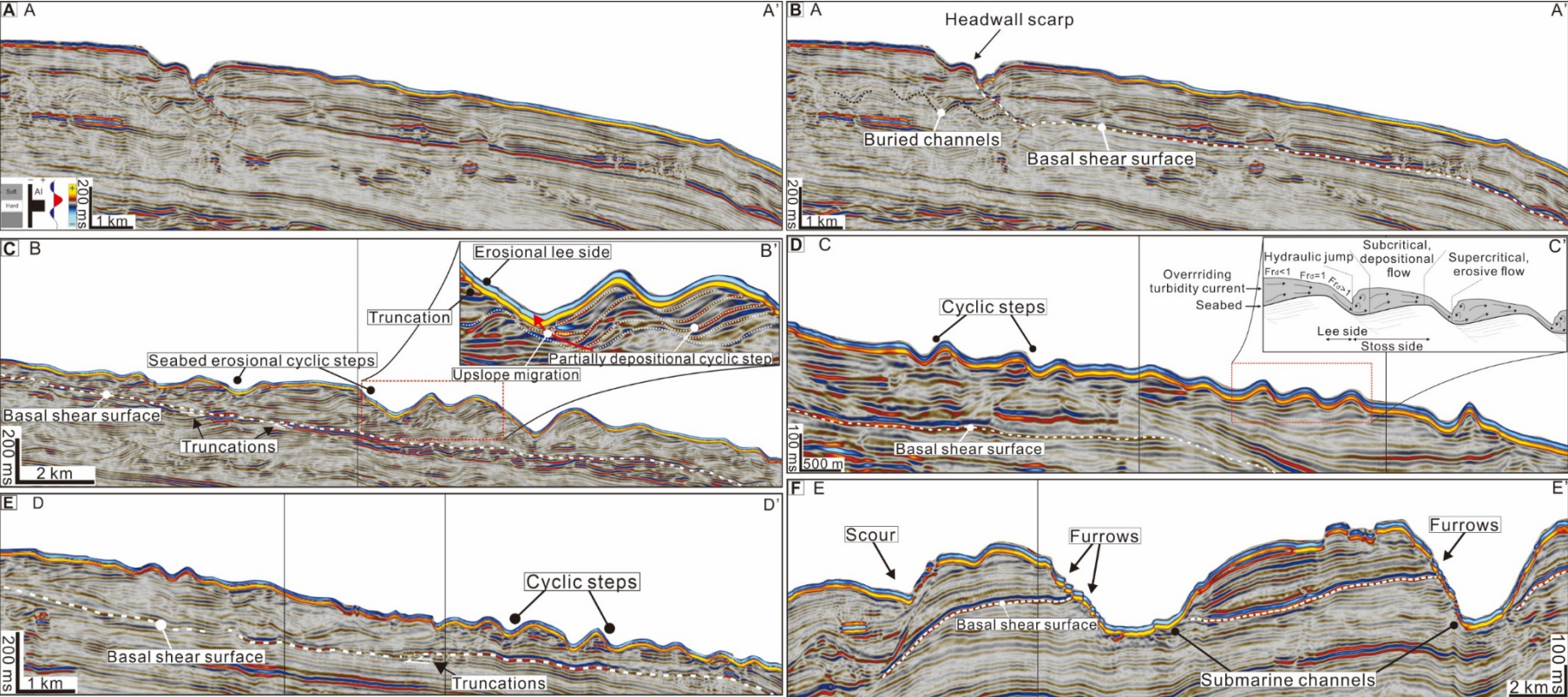


Figure 6

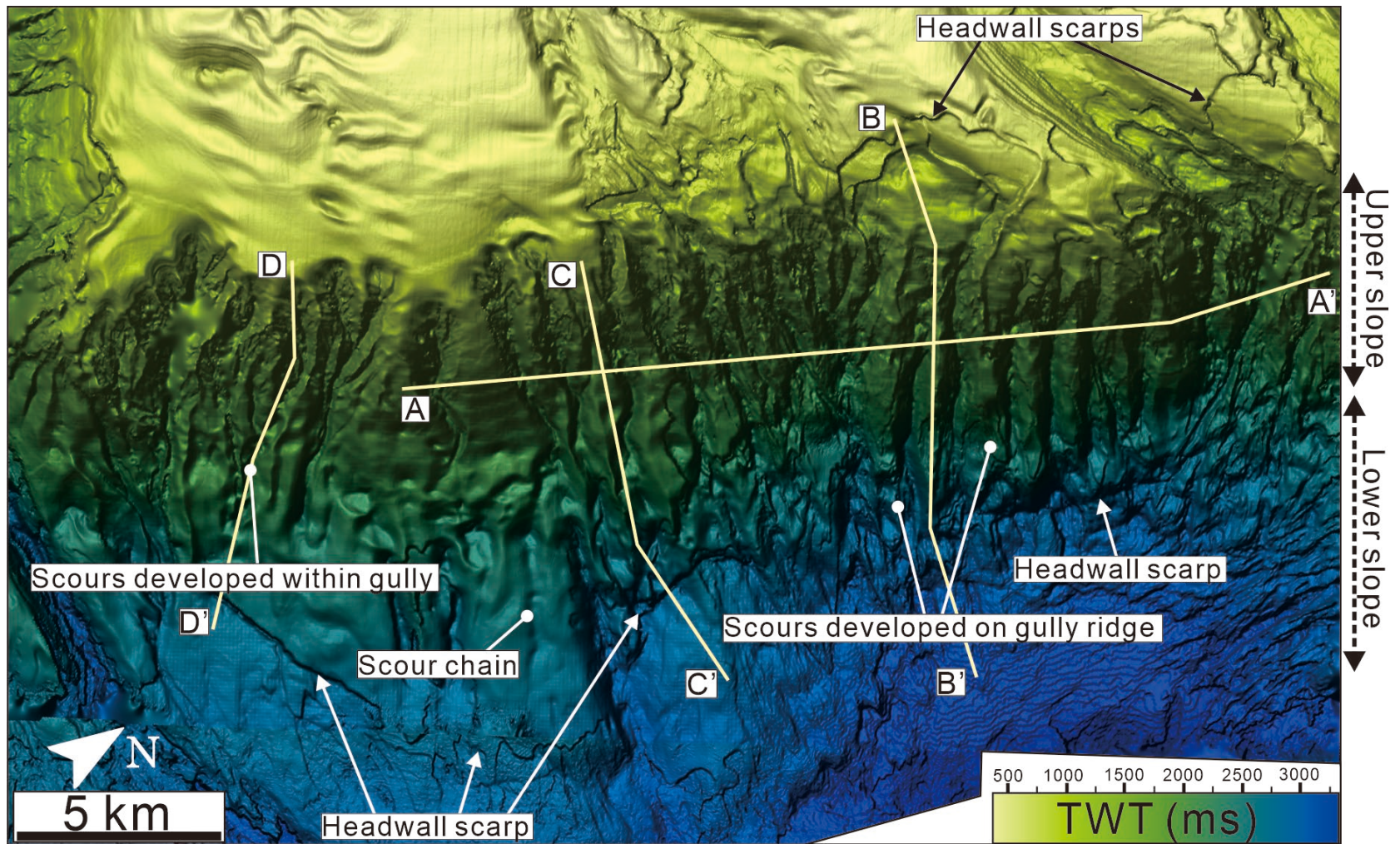


Figure 7

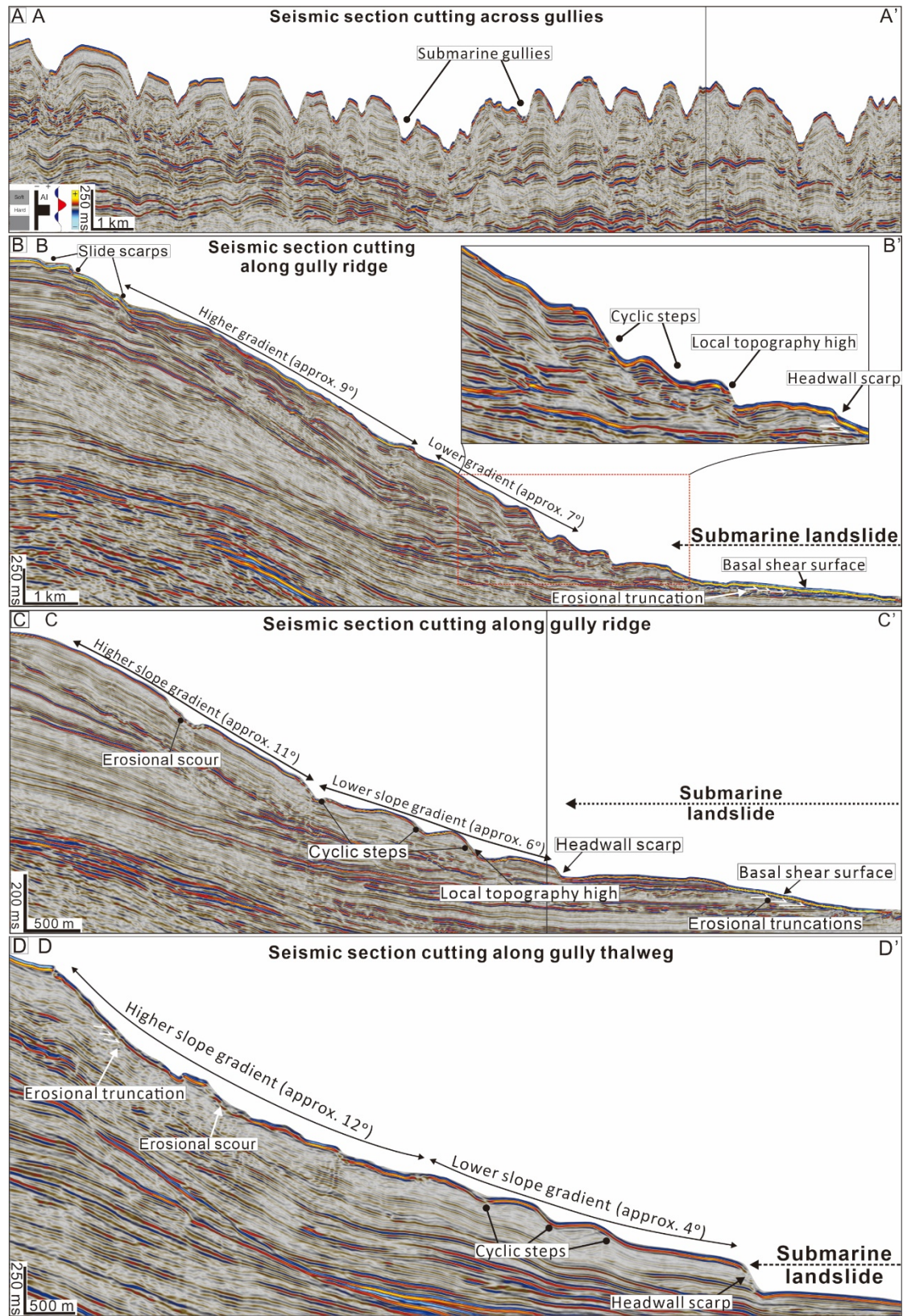


Figure 8

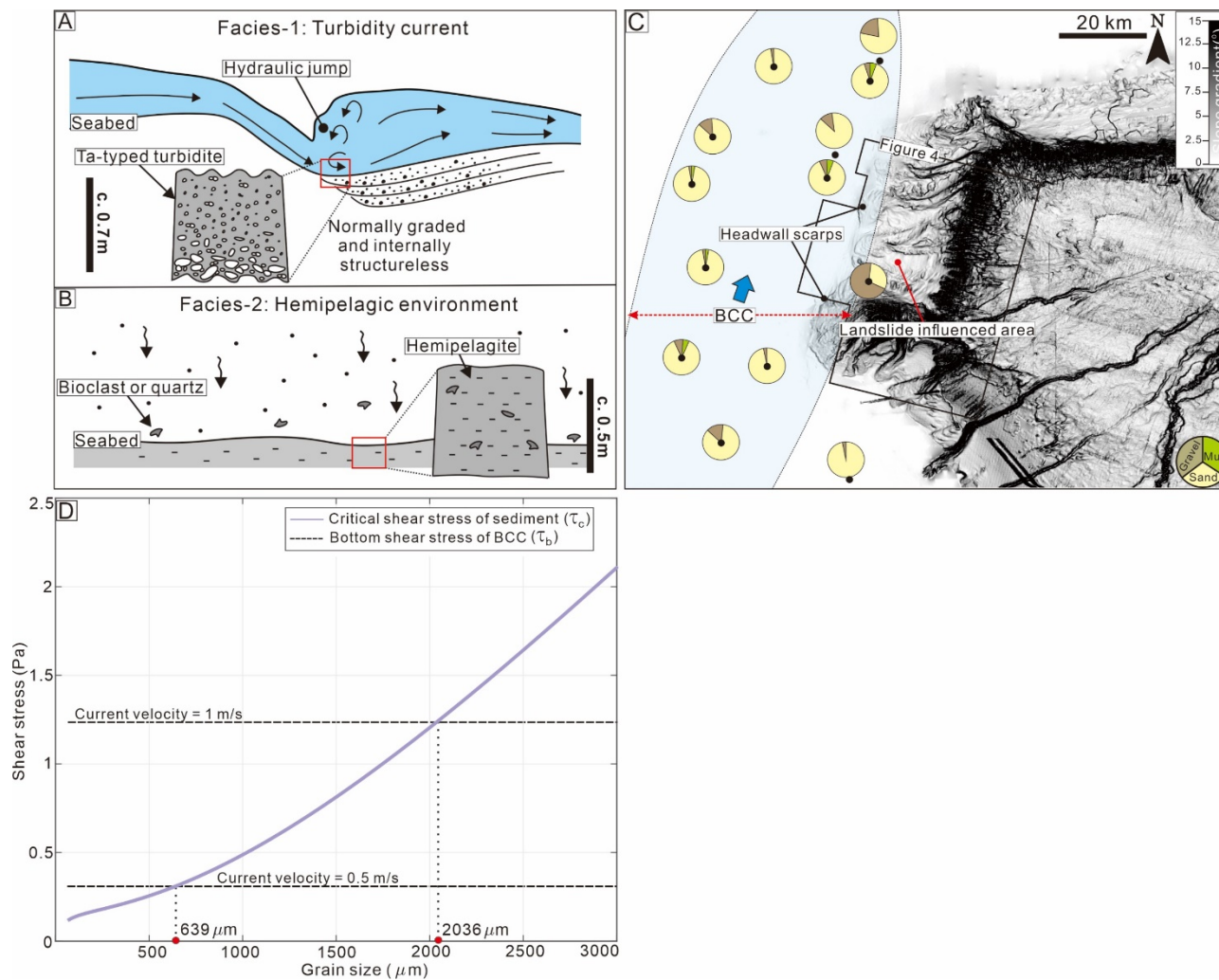


Figure 9

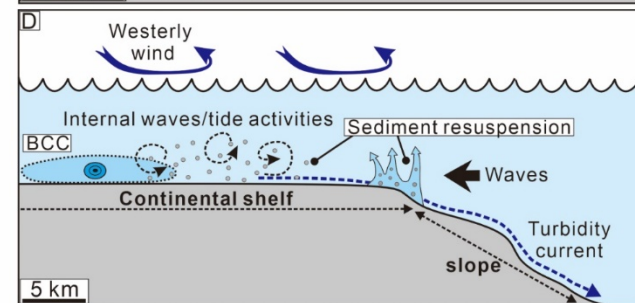
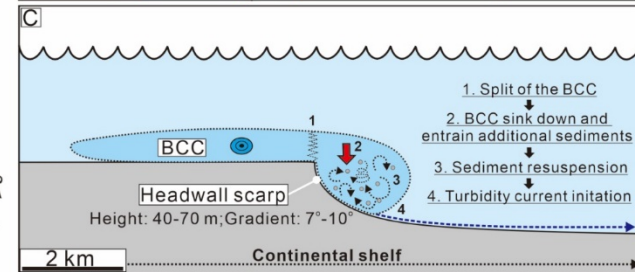
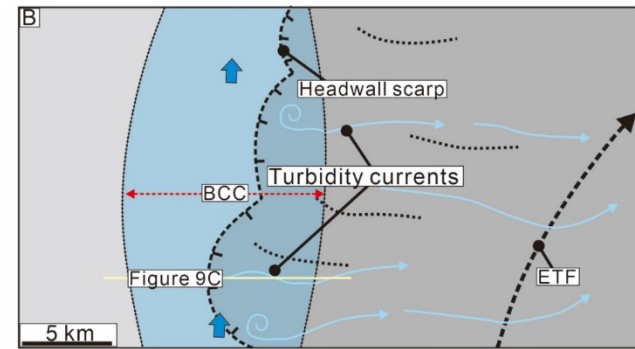
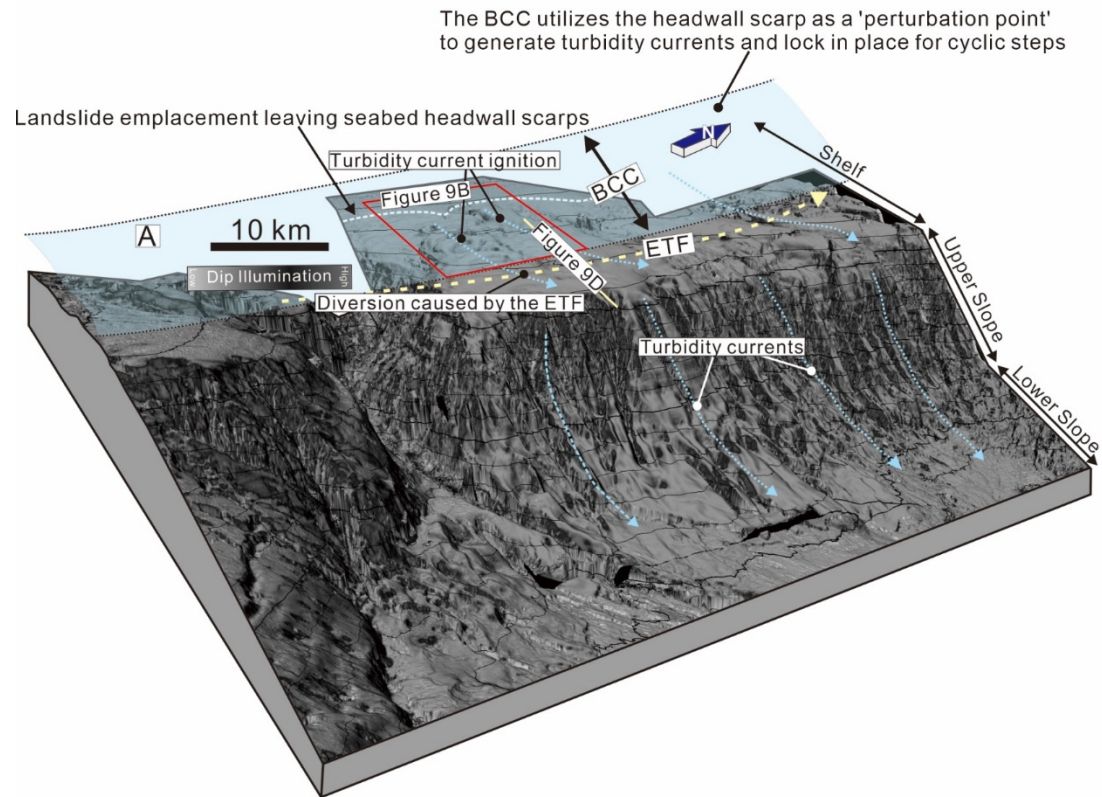


Figure 10

